Room Temperature Micromachined Microbolometers for W-Band (75 GHz -110 GHz) Focal Plane Imaging Array

by

Arifur Rahman

Submitted to the Department of Electrical Engineering and
Computer Science
in partial fulfillment of the requirements for the degree of

Master of Science

at the

MASSACHUSETTS INSTITUTE OF TECHNOLOGY

June 1996

Author . . . .
Department of Electrical Engineering and Computer Science
May 13, 1996

Certified by. . .
Qing Hu
Associate Professor of Electrical Engineering and Computer Science
Thesis Supervisor

Accepted by . . . .
F. R. Morgenthaler
Chairman, Departmental Committee on Graduate Students

Room Temperature Micromachined Microbolometers for W-Band (75 GHz -110 GHz) Focal Plane Imaging Array

by

Arifur Rahman

Submitted to the Department of Electrical Engineering and Computer Science
on May 13, 1996, in partial fulfillment of the
requirements for the degree of
Master of Science

Abstract

This thesis explores the design, fabrication and characterization of uncooled micromachined Nb microbolometers fabricated on a $1-\mu m$ thick Si_3N_4 membrane. The microbolometer consists of a $10 - 30$ nm thick, $5 - 10$ μm^2 Nb strip that acts as a radiation absorber and temperature sensor. Incident radiation is coupled into the microbolometer by a 0.37λ dipole antenna which is placed inside a pyramidal cavity formed by anisotropically etched Si wafers. The center frequency of the micromachined horn antenna is 95 GHz with a 3 dB bandwidth of 15%. The Nb strip is impedance matched with the dipole antenna to reduce the RF reflection loss.

The bolometer theory and the design rules for developing mm-wave focal plane imaging arrays are presented in this thesis. The mm-wave micromachined microbolometers are compact, light weight, and they have a low-cost fabrication process. On chip signal processing and readout circuits can be integrated with them to form monolithic mm-wave detectors and focal plane imaging arrays. Initial measurements of the electrical noise equivalent power (NEP), which defines the sensitivity of these microbolometers are promising, and the NEP can be reduced further by optimizing the geometry of the Si_3N_4 membrane. The frequency response of these devices has $\ln(1/f)$ dependence with frequency and the roll-off frequency is ~ 35 kHz.

Thesis Supervisor: Qing Hu
Title: Associate Professor of Electrical Engineering and Computer Science

Acknowledgments

I have been very lucky to spend the last two years at MIT in a very productive and friendly atmosphere. I am very thankful to my advisor Prof. Qing Hu for providing me this M.S. thesis poject and guiding me throughout the course of this thesis work. I like to thank Earle Macedo, Dan Baker and Bob Konieczka from Lincoln Laboratory (LL) for their technical assistance during the fabrication of the microbolometers and R. Ralston from LL for access to the fabrication facilities in his group.

My research-group members also deserve special mention. I like to thank Gert de Lange for his advice and guidance and making it enjoyable for me to work in this project. Bin Xu, Ilya Lyubomirsky, Farhan Rana, Erik Duerr, Noah Zamdmer, and Simon Verghese deserve special thanks for their suggestions and comments during the experiments. I am also grateful to my parents, brothers, sister, brother- and sister-in-laws, and a very special friend Oni for their support and inspiration in my every day life and in my education.

Contents

.

List of Figures

7

9

List of Tables

.

Chapter 1

Introduction

1.1 Motivation

Over the last few years there has been renewed interest in millimeter-wave ($30\ GHz - 300\ GHz$) devices and technologies for both military and civilian applications [1]. Due to mm-waves ability to penetrate foggy and smoky environments, mm-wave devices are suitable for developing imaging and communication systems for inclement and hazardous weather conditions. The atmospheric windows at $75\ GHz - 110\ GHz$, $130\ GHz - 180\ GHz$ and $195\ GHz - 300\ GHz$ [2] also make many other applications feasible which include remote sensing, satellite communications and collision avoidance radar. For all these applications, it is desirable to have very efficient antennas with high gains, to be used for the transmitter and the receiver. Due to the diffraction limitation, high gain aperture antennas must have dimensions greater than the wavelength corresponding to the carrier wavelength. This can be achieved more easily and at a lower cost in the mm-wave region than the microwave region. Conventional horn antennas with waveguide feeds that have been used widely for mm-wave and microwave devices are very expensive and bulky. They are also incompatible with arrays. To overcome these limitations, micromachining technology have been used to fabricate mm-wave micromachined horn antennas [3, 4, 5, 6]. Active elements of the micromachined horn antennas are fabricated on a $1-\mu m$ thick Si_3N_4 membrane, and their measured antenna gains are greater than $25\ dB$ and the aperture efficiencies are
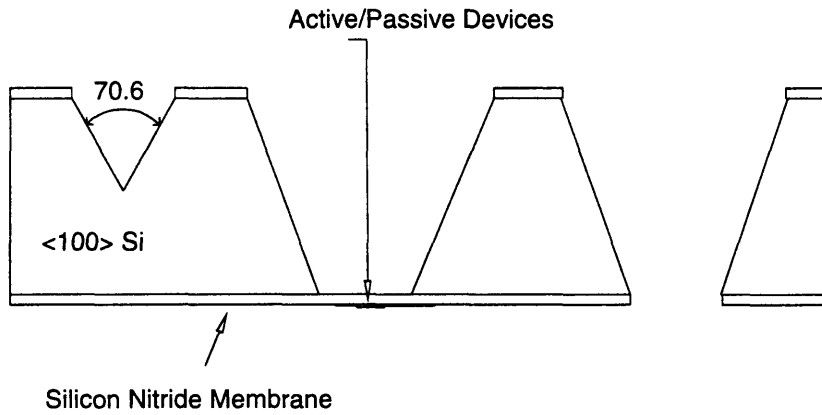
Figure 1-1: Cross sectional view of a micromachined structure etched in ⟨100⟩ silicon.

higher than 90% [6]. Schematic of the Si-micromachined structures which are the building blocks of micromachined horn antennas is shown in Fig. 1.1.

Micromachined horn antennas have several major advantages over the conventional waveguide/horn antennas or substrate supported antennas. Micromachined horn antennas can be fabricated with micron precision on Si or GaAs wafers by using the matured thin-film device fabrication techniques. Other active components, such as RF and IF amplifiers, mixers and local oscillators can also be integrated to form monolithic transmitter/receiver systems. These horn antennas are very compact, and they can be mass-produced at a low cost. Moreover, focal plane arrays can be fabricated easily on a single wafer. Quasi-optical components can also be combined with these micromachined horn antennas to increase radiation coupling efficiency and to collimate the radiating beams. Over the last few years, micromachined horn antennas have been used to fabricate heterodyne receivers such as SIS and Schottky mixers [6, 7, 8] and incoherent/direct detectors such as macro- and micro-bolometers [9, 10]. In these detectors/mixers, radiation is coupled by dipole antennas which are fabricated on a $1-\mu m$ thick Si_3N_4 membrane. For a micromachined microbolometer, the Si_3N_4 membrane provides natural thermal isolation to the temperature sensor (a thin film with an area of $\sim 5 - 10 \ \mu m^2$) which is fabricated on the Si_3N_4 membrane. So, the micromachined structures are ideal for microbolometers.

1.2 Approach

The micromachined microbolometer is composed of a Nb strip that acts as a radiation absorber and a temperature sensor. Bismuth has been the material of choice for this purpose because it has a low electrical conductivity, and therefore, Bi microbolometers can be easily impedance matched with planar antennas. The best reported noise equivalent power (NEP) which defines the sensitivity of a microbolometer is approximately 4×10^{-11} $W/Hz^{1/2}$ at a modulation frequency of 50 kHz for uncooled air-bridge Bi microbolometer [11]. However, Bi and other semimetal films are known to have a high level of 1/f noise [12]. This is the reason why the good NEP of the Bi microbolometers can be achieved only at an inconvenient 50 kHz modulation frequency. It has been shown recently that the 1/f noise of niobium films is much lower than that of the bismuth films [13]. Moreover, $15 - 30$ nm thick Nb films provide the desired impedance matching with planar antennas. With uncooled antenna-coupled Nb microbolometers fabricated on thermally grown SiO_2 layers on Si wafer, NEP as low as 1.1×10^{-11} $W/Hz^{1/2}$ has been achieved [13]. We have combined the low 1/f noise property of the Nb films with the compact size and high gain of micromachined horn antennas to fabricate micromachined Nb microbolometers.

For an antenna-coupled microbolometer on a thin membrane with its dimensions and geometry optimized so that most of the thermal conduction is through the antenna leads, the lower limit of NEP is set by the phonon noise, or noise due to temperature fluctuations. It is given by $\sqrt{4kG_aT}$ [14], where $k = 1.38 \times 10^{-23}$ J/K is the Boltzman constant, $T = 300$ K is the operating temperature, and G_a is the thermal conductance of the antenna leads. For typical metallic antenna leads with a resistance of $\simeq 3$ Ω, we obtain a thermal conductance of 2.44×10^{-6} W/K from Widemann-Franz law [15]. The corresponding lower limit of NEP is 3.5×10^{-12} $W/Hz^{1/2}$, which is two orders of magnitude lower than that of the commercial pyroelectric detectors [16].

Our goal for this project is to achieve NEP as low as possible by using Si micromachining techniques. First, we will fabricate the micromachined Nb microbolome-

13

ters on a 0.509λ square and $1-\mu m$ thick Si_3N_4 membrane and characterize them. For this geometry of the microbolometer, thermal conductance of the membrane ($\sim 2 \times 10^{-5}$ W/K) is greater than the thermal conductance of the antenna leads [10]. Also, for a typical microbolometer with a resistance of ~ 30 Ω, the contribution from the Johnson noise ($\sim 2 \times 10^{-10}$ $W/Hz^{1/2}$) to the NEP is much greater than the phonon noise limited NEP. So, we have to optimize the geometry of the Si_3N_4 membrane to reduce its thermal conductance and increase the microbolometer's sensitivity. This can be accomplished by etching away part of the membrane not directly below the microbolometer and the dipole antenna. Once we are successful in optimizing the sensitivity of the microbolometer, we would like to design and fabricate mm-wave focal plane imaging arrays using these uncooled microbolometers. In future, we intend to integrate readout and signal processing circuits with the focal plane arrays to form monolithic imaging systems.

1.3 Overview of this Work

In Chapter 2, bolometer theory and design issues for the focal plane imaging arrays are presented. Fabrication process of the micromachined microbolometer is discussed in Chapter 3. Some of the critical fabrication steps are also emphasized. Chapter 4 provides all the experimental results for the Nb microbolometer. These experimental results contain both DC and RF measurements that are performed to characterize the microbolometer.

Chapter 2

Theory: Bolometric Detection and The Imaging Array

This chapter provides the necessary background needed to understand the radiation detection mechanism of bolometers and to optimize their sensitivities. In section 2.1, a brief description of the microbolometer used in this project and how it functions are presented. Discussions on the various types of noise sources that degrade the sensitivity of the bolometers are given in section 2.2. This chapter ends with some design issues for the microbolometer-focal plane imaging arrays for active (radar) and passive (radiometric) imaging which is given in section 2.3.

2.1   Bolometer Theory

Bolometer is a square law thermal detector where the output signal (current or voltage) is proportional to the input signal (electromagnetic radiation intensity). It consists of a radiation absorber and a temperature sensor with a heat capacity C, and it is connected to a heat sink at temperature T_0 via thermal conductance G_t. When an incident radiation power ΔP is applied, it induces a change in temperature in the bolometer from T_0 to $T_0 + \Delta T$. Due to this temperature variation, the resistance of the bolometer changes, and by measuring the change in resistance, one can deduce the intensity of the detected electromagnetic radiation. If the incoming radiation is

modulated at a frequency f, the heat balance equation is [17]:

$$j2\pi fC\Delta T + G_t(f)\Delta T = \eta\Delta P, \tag{2.1}$$

where η is the optical coupling efficiency of the bolometer. For a bolometer biased at a DC voltage V_b, the change is voltage ΔV across the bolometer due to the incident radiation is $\alpha V_b\Delta T$ where $\alpha = (1/R \cdot dR/dT)$ is the temperature coefficient of resistivity. By eliminating ΔT from Eq. 2.1, we get

$$\Delta V = \eta\frac{\alpha V_b\Delta P}{G_t(f) + j2\pi fC}. \tag{2.2}$$

Though ΔV is proportional to the bias voltage, V_b cannot be increased indefinitely. The maximum bias voltage that can be applied is limited by the excessive Joule heating in the bolometer. It is reasonable to assume that the resistance of the bolometer can be expressed as $R \simeq R_0 + \beta P$, where P is the power dissipated in the bolometer and β is a constant. Then it can be shown that the thermal runway will occur at a bias current $\sqrt{1/\beta}$ [13]. This corresponds to a maximum applicable bias voltage $V_b \simeq R_0/\sqrt{\beta}$.

The voltage responsivity of the bolometer is defined as $S(f) = \Delta V/\Delta P$ and its response time is $\tau \simeq C/G_t(0)$. For bolometers, $1/\tau$ is too small for heterodyne mixing with useful intermediate frequency (IF) bandwidths. In most of the room and low temperature applications, bolometers are used as direct (active or passive) detectors. However, it has been proposed that superconducting transition edge microbolometers can be used for terahertz mixing with usable IF bandwidth of several GHz, which agrees with the theoretical prediction [18]. Experimental results on superconducting microbolometer mixers are presented in Ref. [19]. In a superconducting hot-electron microbolometer mixer, electron-electron interaction is enhanced due to the high surface scattering compared to the electron-phonon interaction. The response time is determined by the rapid diffusion of hot electrons to the heat sink. With the superconducting hot-electron microbolometers, usable IF bandwidths as high as $1\ GHz - 10\ GHz$ can be achieved [20]. Currently, superconducting microbolome-

ters are considered seriously for heterodyne mixing in the terahertz region where SIS (superconductor-insulator-superconductor) and Schottky diodes are difficult to fabricate.

The response time of the bolometer can be reduced by reducing the dimensions of the bolometer. Microbolometers have dimensions much smaller than the wavelength, and they have very small response time [11]. Incident radiation is coupled into the microbolometer by a lens, planar antenna or a lens-antenna structure [10, 13, 17, 21]. Planar microbolometers are fabricated on high thermal resistance substrates to provide good thermal isolation to the microbolometers [11]. Another approach to provide sufficient thermal isolation is to use the air-bridge technique [22]. Air-bridge microbolometers are suspended on air above the substrate, and the only thermal conduction path is through the bias contact leads. Recently, Nb microbolometers have been also fabricated on thermally grown thin SiO_2 layers on Si substrate [13]. The thin SiO_2 layer improves the thermal isolation of the microbolometer. Sensitivity of these Nb microbolometers is comparable to that of the air-bridge Bi microbolometers. Our approach for providing good thermal isolation is by fabricating the microbolometer on a thin Si_3N_4 membrane using Si micromachining technique. The radiation coupling structures consist of a micromachined pyramidal horn and a 0.37λ dipole antenna. So far, we have obtained very promising results with the Nb micromachined microbolometer [10].

For an antenna-coupled micromachined microbolometer (as shown in Fig. 2-1) fabricated on a thin membrane, $G_t(f) = G_m(f) + G_a(f) + G_c(f)$, where $G_m(f)$ and $G_a(f)$ are the thermal conductance of the membrane and the antenna leads, and $G_c(f)$ is the thermal conduction due to heat convection to air. To evaluate G_m for a square membrane, we model the rectangular microbolometer on top of the membrane of thickness t as an isotropic disk of radius r_1 such that $2\pi r_1$ is equal to the circumference of the the microbolometer, and the heat flow is in the radial direction. The DC thermal conductance of the membrane is found from the 2D Laplace's equation, and is given by:
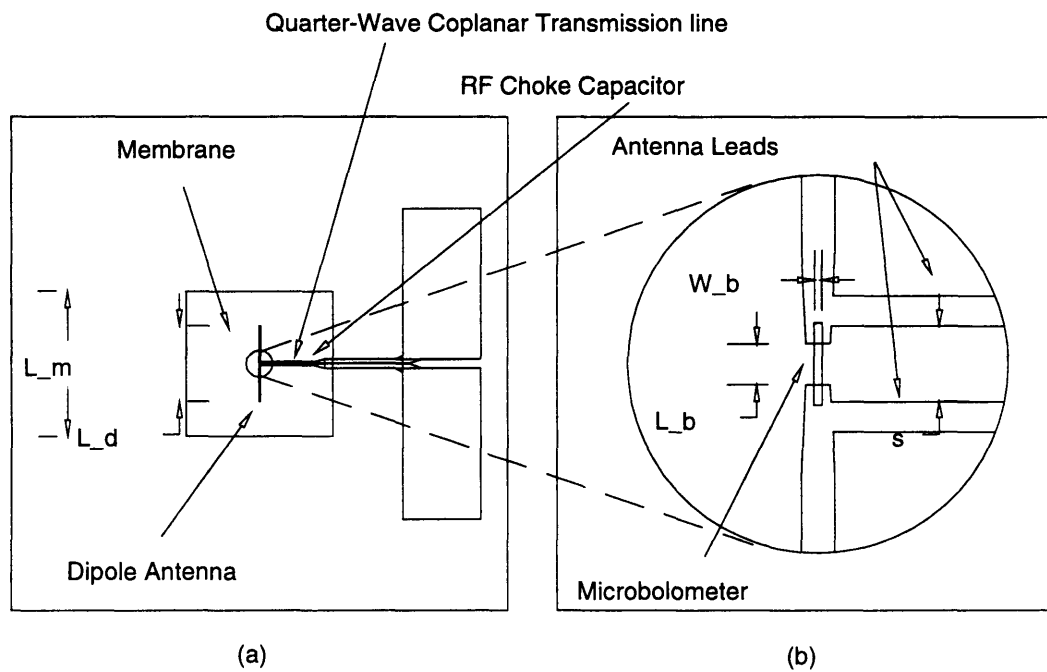
Figure 2-1: (a) Antenna-coupled microbolometer on a thin membrane. In this figure, $L_m = .509\lambda$ and $L_d = .37\lambda$ (b) magnified schematic of the microbolometer and the antenna leads. The dimensions of the microbolometer are $3.2\mu m$ $(W_b) \times 2\mu m$ (L_b), and the separation between the coplanar transmission lines is $s = 10\mu m$.

$$G_m(0) = 2\pi\kappa_m t(ln\frac{r_2}{r_1})^{-1}, \tag{2.3}$$

where, κ_m is the thermal conductivity of the Si_3N_4 membrane, and r_2 is half of the width of the square membrane. The temperature change at a finite modulation frequency follows from the expression of a 2D point source located at the center of the membrane [23]:

$$\Delta T(r, f) = \frac{1}{2\pi\kappa_m t}K_o(\sqrt{\frac{i2\pi f}{\kappa}}r)\Delta P, \tag{2.4}$$

where $\kappa = \kappa_m/H_m$. H_m is the specific heat of Si_3N_4, and $K_0(x)$ is the modified Bessel function [24]. For numerical calculations, it is convenient to use $K_o(x) = ker(x) + ikei(x)$ [24]. The analytical expressions of $ker(x)$ and $kei(x)$ are given in appendix A.

The frequency dependent thermal conductance of the two gold antenna leads can be found by solving the one-dimensional thermal diffusion equations for a rectangular bar where the temperature variation is only along the longitudinal direction. For a bar with a width, thickness and length w, t_a, and l, respectively, it is :

$$T(z) = \frac{T_0 \cdot \cosh(z/L - l/L)}{\sinh(l/L)}, \tag{2.5}$$

where, $L = \sqrt{\kappa_g/j2\pi f H_g}$ is the thermal diffusion length, κ_g and H_g are the thermal conductivity and specific heat of gold. The thermal conductance is given by

$$G_a(f) = \kappa_s(\Delta T)^{-1} \int \nabla T \cdot dS, \tag{2.6}$$

and using Eq. 2.5 and 2.6, we get $G_a(f) = (\kappa_g w t_a/L) \cdot \coth(l/L)$. In the limit $f \to 0$, the DC thermal conductance is given by $G(0) = \kappa_g w t_a/l$. The DC thermal conductance can also be calculated by using the Widemann-Franz law which relates the electrical conductivity to the thermal conductivity [15] in the following manner:

$$\frac{\kappa}{\sigma T} = Lorenz\ Number = 2.44 \times 10^{-8}\ W - \Omega/K^2, \tag{2.7}$$

19
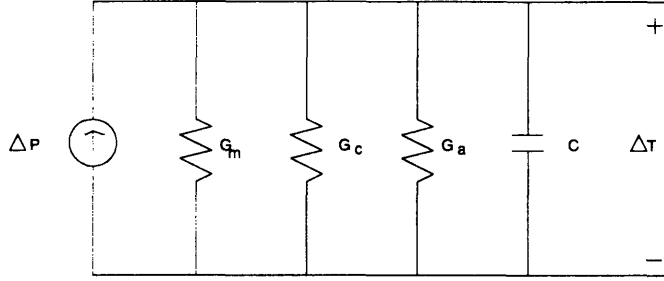
Figure 2-2: Equivalent thermal circuit model of a microbolometer. Incident power ΔP induces a change in temperature ΔT on the bolometer; ΔT and ΔP can be measured with a calibrated bias circuit.

where κ and σ are the thermal and electrical conductivity, respectively, and T is the temperature.

The thermal conductance due to convection is given by $G_c(f) \simeq h_c L_m^2(f)$, where h_c is the coefficient of the area-thermal conductance of air $(3 - 14 \; W/m^2K)$ [25] and $L_m(f)$ is the thermal diffusion length in the membrane. An equivalent circuit model of the microbolometer in terms of the thermal conductance is shown in Fig. 2-2. For the Nb microbolometer on thin membrane, because of its small C ($\simeq 2.9 \times 10^{-13} \; J/K$), the 1st term in the denominator of Eq. 2.2 dominates over the 2nd term in the frequency range of interest, where we have assumed $G_m \geq 2 \times 10^{-5} \; W/K$, $G_a \geq 3 \times 10^{-6} \; W/K$, and $G_c \leq 6.4 \times 10^{-6}$ for typical device geometries. So, the response time is dictated by the frequency dependence of $G_t(f)$, and it is larger than $\simeq C/G_t(0) \simeq 0.015 \; \mu sec$.

2.2 Noise Equivalent Power

Noise Equivalent Power(NEP) represents the sensitivity of a microbolometer. It is defined as the minimum detectable signal power for a 1 sec. integration time. Summing up the contributions of all noise sources in quadrature we get [14]:

$$NEP = [4kT^2G_t + \frac{4kTR}{S^2} + \frac{e_n^2 + (i_nR)^2}{S^2} + \frac{e_{1/f}^2}{S^2}]^{\frac{1}{2}}. \tag{2.8}$$

20

The first term in Eq. 2.8 is the phonon noise term and the second term is due to the Johnson noise; e_n and i_n are the noise voltage and noise current of the amplifier, and $e_{1/f}$ is the $1/f$ noise voltage of the bolometer.

The phonon noise is due to the energy fluctuation of the microbolometer which is connected to a heat sink at a temperature T_0 via thermal path with thermal conductance G_t. Physically, this noise arises due to the number fluctuation of the quantized carriers of energy (phonon/electrons) through the thermal conductance path [14]. The contribution from all noise sources besides the phonon noise term can be minimized by optimizing the responsivity of the bolometer. So, the fundamental limit of NEP is set by the phonon noise, which is also called thermodynamic noise limit.

Johnson or Nyquist noise describes the fluctuations in voltage across a dissipative circuit element due to the thermal motion of charge carriers [26, 27, 28]. For a resistor with a resistance R, the Johnson noise voltage is $\sqrt{4kTR\Delta f}$, where k is the Boltzman's constant, T is the temperature and Δf is the system bandwidth.

The noise in an amplifier is represented by a noise voltage and a noise current terms. The noise voltage includes the contribution from the Johnson noise and $1/f$ noise sources of the amplifier's circuit elements, and the noise current represents the shot noise due to the diode leakage currents. Both noise current and noise voltage depend on the amplifier's bias point. Monolithic operational amplifiers (op-amps) are generally optimized for low power rather than for low noise. Besides, the users don't have much control over the bias point of the monolithic amplifiers. So, for low noise applications with source resistance $R_s \sim 10 - 1000$ Ω, it is recommended to use low noise bipolar junction transistors (BJT) or junction field effect transistors (JFET) as the first stage of the amplifying circuits, followed by further amplification by op-amps. By choosing the bias point of the BJTs and JFETs, optimum noise voltage or noise current can be achieved for a given application. The dependence of noise voltage or current on bias point and frequency for BJTs or JFETs can be found in Ref. [29]. The noise model of an amplifier connected with a resistor R_s, and the total noise for various source resistance are shown in Fig. 2-3.

At low values of source resistance, amplifier's noise voltage E_n alone is important.
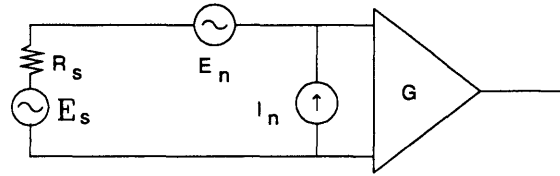
(a)
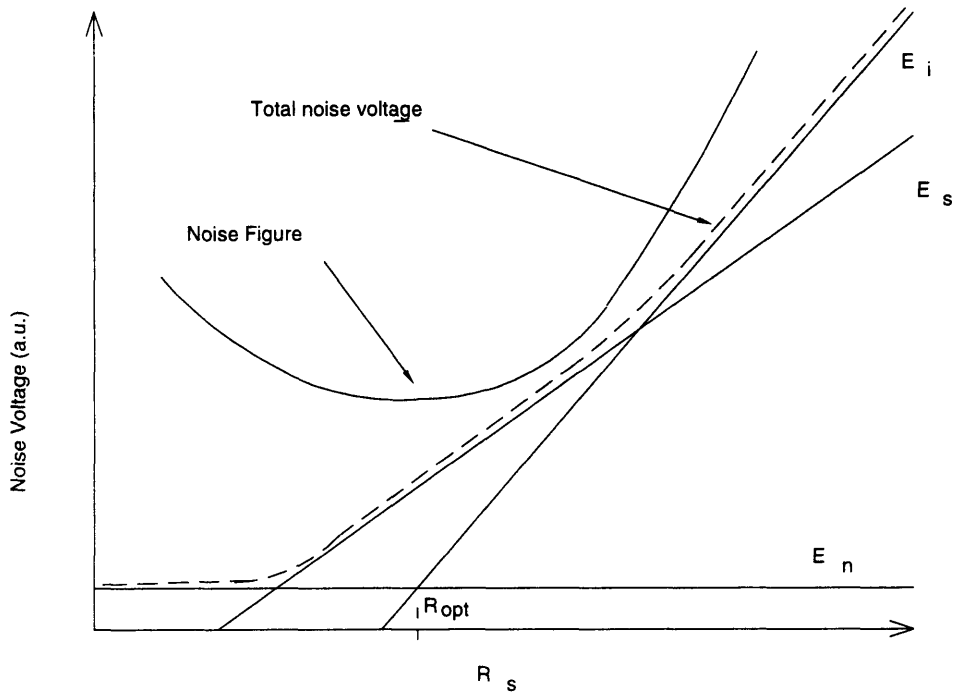
(b)

Figure 2-3: (a) Noise model of a resistor connected with an amplifier with gain G. The total output noise voltage is $E_{out} = G \cdot [(I_n R_s)^2 + E_n^2 + E_s^2]^{1/2}$, where E_s is the thermal noise of the resistor. (b) Plot for the noise voltages and NF vs. source resistance for the configuration shown in Fig. (a). The NF is minimum for $R_s = R_{opt} = E_n/I_n$.
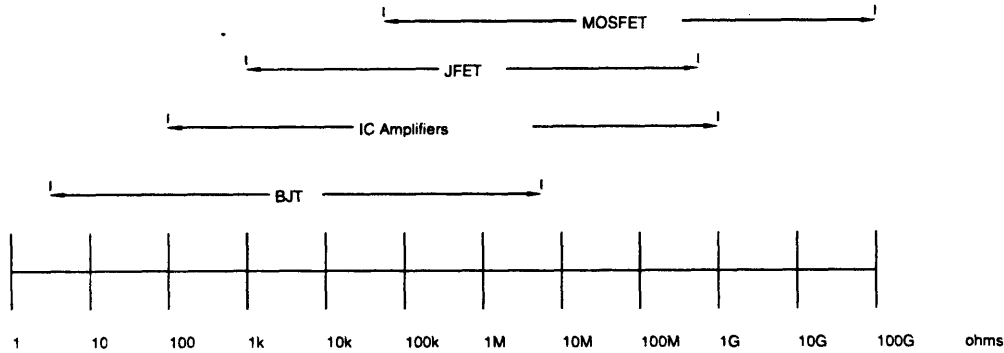
Figure 2-4: Recommended amplifying circuit elements for low noise applications for various ranges of source resistance.

As the source resistance increases, $E_i = I_n R_s$ cannot be neglected anymore; with even higher values of R_s, E_i becomes the dominating noise term. A low noise amplifier is often characterized by its noise figure (NF). NF is defined as [30]:

$$NF = 20 \log(\frac{total \; output \; rms \; noise \; voltage}{gain \; \times \; source \; thermal \; noise \; voltage}) \qquad (2.9)$$

It can be shown very easily that the NF is minimum when $R_s = E_n/I_n$. In other words, for this value of source resistance, the amplifier adds minimum noise to the thermal noise of the source. A list of various types of circuit elements recommended for the construction of low noise amplifiers in different source resistance ranges is summarized in Fig. 2-4 [30].

The noise spectral density of the $1/f$ noise is proportional to $f^{-\alpha}$, where α is close to unity. Over the years, several models have been proposed to theorize the $1/f$ noise [12, 28, 31, 32, 33] and its origin. The noise spectra due to the charge carriers' number and mobility fluctuations have a $1/f$ dependence [28]. It has been also proposed that the $1/f$ noise is associated with the defect motion in metallic films [31, 34, 35] and annealing can have substantial effect on the $1/f$ noise properties [34]. $1/f$ noise is a current induced noise that dominates, specially, at low frequencies [32]. Thermocouple, a type of thermal detector, which does not require any biasing is free from $1/f$ noise [11]. The magnitude of the $1/f$ noise voltage increases with the bias

current, and roughly, it is proportional to the bias current. Even after many years of research efforts, $1/f$ noise still remains as one of the elusive phenomena in solid state physics.

2.3   Coupling of the Millimeter Waves to the Microbolometer

The general criteria for a good mm-wave coupling structure include:

a) high coupling efficiency

b) low cross-polarization levels

c) high gain

d) and high directivity.

For focal-plane array applications, it is also desirable to have a high packaging density. Moreover, for large scale production, the fabrication process of the coupling structures should be inexpensive and simple. It is also important to have a high coupling efficiency to the fundamental Gaussian mode because the lowest order Gaussian mode is capable of propagating through the quasi-optical components nearly without any loss.

Generally, radiation is coupled into the microbolometers with planar antennas and substrate lenses [13, 17, 21]. Waveguide-horn structures can also be used instead of planar antennas. Planar antennas suffer from the dielectric losses and radiation loss due to the trapped waves in the substrate [21]. Waveguides are also difficult to fabricate in the sub-millimeter wavelengths. Micromachined horn structures are appropriate for microbolometers and integrated circuit technologies. They are compact and inexpensive and have a very high coupling efficiency. We use a 0.37λ dipole antenna fabricated on a $1-\mu m$ thick Si_3N_4 membrane and placed in a Si micromachined horn cavity to couple the electromagnetic radiation. The microbolometer is also fabricated on the same membrane. The thin membrane provides a very good thermal
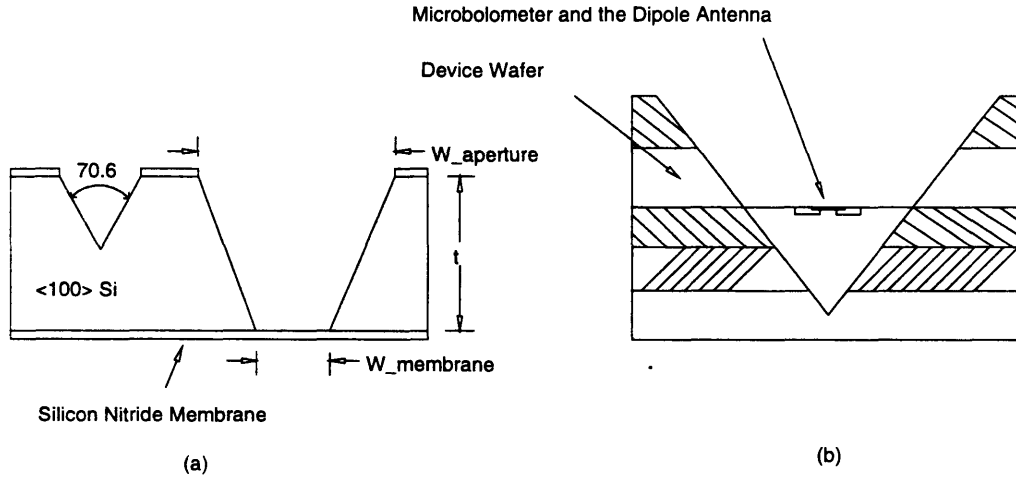
Figure 2-5: (a) Micromachined Si wafer and (b)the pyramidal horn cavity.

isolation between the microbolometer and its surrounding; it also eliminates the radiation loss to the substrate and reduces the excitation of surface waves. This type of micromachined horn antennas were first developed at the University of Michigan and have been used for Schottky and SIS receivers [4, 6, 7, 8, 36].

The micromachined horn cavity as shown in Fig. 2-5 is created by stacking four to five anisotropically etched Si wafers. KOH etches the $\langle 100 \rangle$ silicon approximately 400 times faster than the $\langle 111 \rangle$ silicon, and the pyramidal cavity is formed by the $\langle 111 \rangle$ crystal planes. For the Si micromachined structure shown in Fig. 2-5(a), $W_{aperture} = W_{membrane} + t\sqrt{2}$ [37]. The flare angle of 70^0, inherent to the $\langle 111 \rangle$ crystal planes is too large for any useful application. The large flare angle limits the antenna gain to less than 13 dB and the 10-dB beamwidths greater than 90^0 [5]. In order to reduce the flare angle and improve the Gaussian beam coupling efficiency, a machined horn is placed in front of the micromachined section. The abrupt change in flare angle from the micromachined to the machined horn section also acts as a mode converter that excites mainly the $TE_{10}, TE_{12}, TM_{12}$ and TE_{30} modes. The length of the machined section is chosen such that all the modes that are excited in the cavity and propagate through the horn, interfere with each other to produce a highly symmetrical far-field pattern with high gain. The choices of the length and the flare angle of the machined section are critical for obtaining a high coupling efficiency. A

25
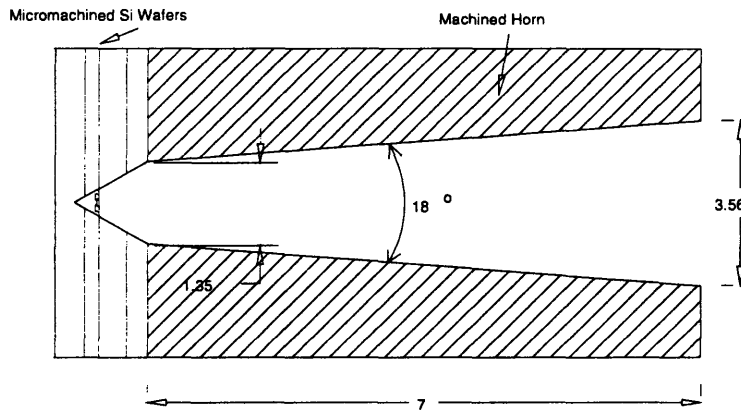
Figure 2-6: Micromachined horn structure for mm-wave detection. All units are in wavelength.

schematic of the horn structure is shown in Fig. 2-6.

The pattern produced by such a horn has [6]:

a) 20 dB antenna gain

b) 97% Gaussian coupling efficiency

c) 34^0 10 dB-beamwidth

d) -27 dB E-plane sidelobe level

e) and -22.7 dB cross polarization level.

The phase center of this type of horn antenna is 1.45λ inward from the machined aperture. The beam pattern of the micromachined horn antenna is shown in Fig. 2-7 [38].

The position of the feed (the dipole antenna) from the apex of the horn is very critical in determining the impedance seen by the dipole antenna. If the dipole is placed close to the apex where the width of the cavity is less than half a wavelength, only evanescent modes will be excited, and the modal amplitudes of the excited modes will decay very fast before reaching the aperture. When the dipole lies outside the cut-off region, TE_{mn} modes ($m = 1, 3, 5..., n = 0, 2, 4...$) and TM_{mn} modes ($m = 1, 3, 5..., n = 2, 4, 6...$) are excited. If the dipole is placed close to the largest micromachined aperture, higher order modes can propagate through the horn and

26
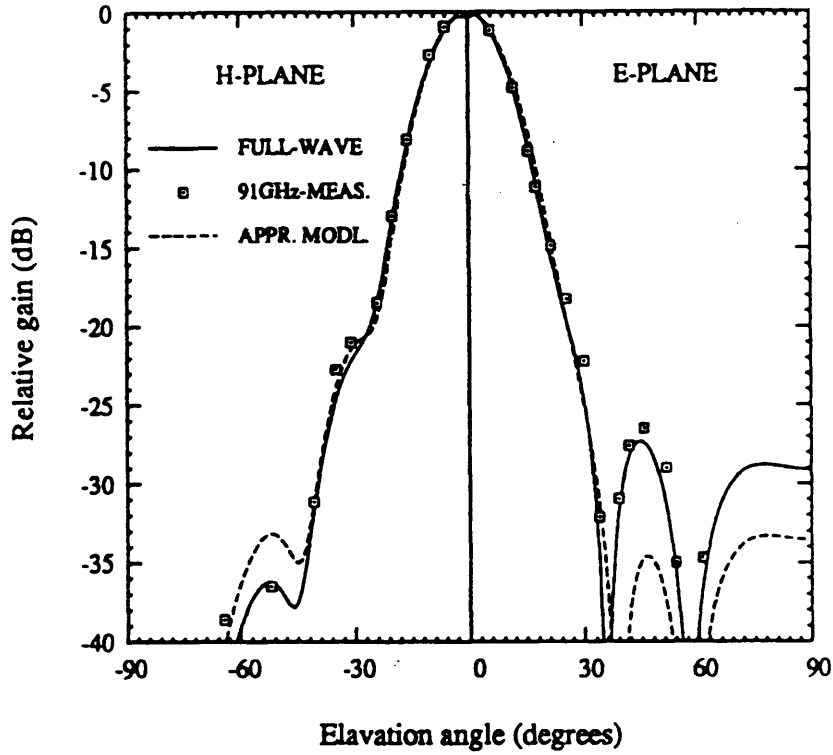
Figure 2-7: Antenna pattern of a micromachined horn antenna [38].

distort the beam pattern and reduce the directivity. We place the dipole antenna 0.36λ away from the apex, and the corresponding antenna impedance is 35 Ω [39]. The impedance of the microbolometer should match the dipole impedance, to reduce the radiation coupling loss, and it can be achieved easily with a 10 nm − 20 nm thick Nb film of an aspect ratio (length/width) $\simeq 2 - 3$.

2.4 Imaging Array

Imaging is the process of gathering radiation arriving from different angles and the analyses of the detected signals to extract information about a target or a scene. Imaging can be done with a single or multiple detectors. However, there are many advantages in using multiple detectors or arrays over a single detector. An array of detectors can reduce the integration time to build up an image and increase the overall sensitivity of any detection mechanism. For an array with N elements. the integration time is reduced by a factor of N, and the sensitivity is increased by a

factor of $\sqrt{N}$ compared to a single detector [40]. Imaging using a single detector has to rely on mechanical scan.

There are several ways an image of a scene or target can be mapped. For a single receiver imaging, the receiver is either moved in the focal plane of a radiating aperture (parabolic dish or lens), or the direction of the beam is scanned mechanically or electrically. But this is a very slow and cumbersome process. Phased array antennas can also be used for mm-wave imaging. In phased-array imaging system, the signals from different receivers are analyzed in a way such that the phased-array is sensitive to beams arriving from different directions. Interferrometric arrays, where the signals from different receivers are correlated to map out a scene are mainly used in astronomy. Our approach to mm-wave imaging is with an array of bolometric detectors placed at the focal plane of a radiating aperture (a thin lens or a parabolic dish). The image is sampled at the focal plane of the lens (or the parabolic dish) and later reconstructed by taking a spatial Fourier transform. In Fig. 2-8, the imaging mechanism of a focal plane imaging array is illustrated, where each detector in the focal plane samples a different point of a scene.

There are several requirements for an imaging array in order to image an object efficiently. Failure to meet these requirements may deteriorate the resolving power of the imaging array. These requirements are:

a) efficient aperture illumination

b) proper sampling interval in the focal plane

c) and high coupling efficiency to the active elements/devices.

The imaging array should dissipate low power and for antennas on substrates, the radiation loss must be minimum. The off-axis aberration should also be as small as possible.
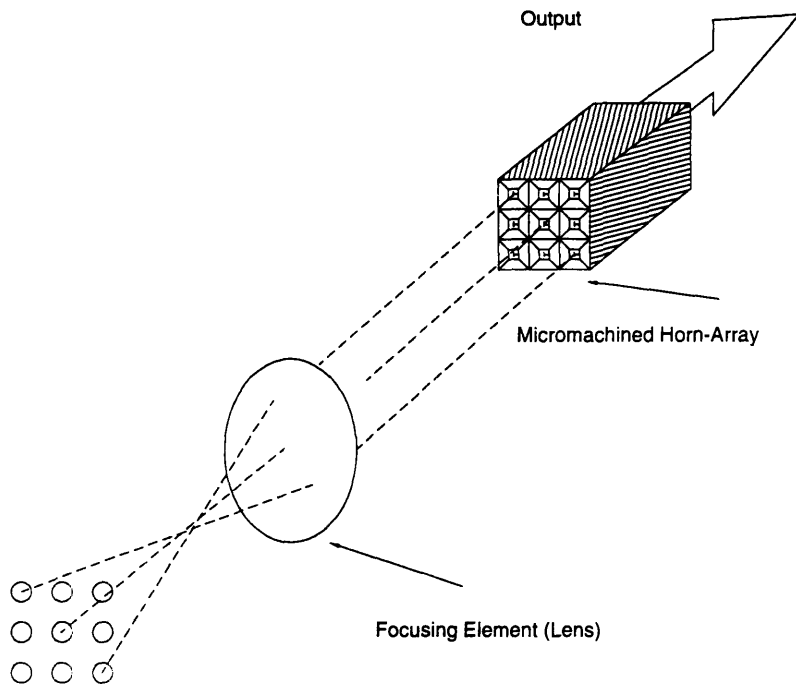
Figure 2-8: Schematic of a focal plane imaging array where each pixel of the array images a different point of the scene or target.

2.4.1 Aperture Efficiency

A good aperture illumination efficiency requires low sidelobe levels of the radiated beams. Most of the conventional feeds rectangular, conical or corrugated horns used in imaging arrays have high Gaussian coupling efficiency, and acceptable sidelobe levels. The micromachined horn that we use has a -27 dB sidelobe level in the E-plane and a very high coupling efficiency [6]. The aperture illumination efficiency of a lens-antenna system is a function of relative illumination at the edge of the lens (edge taper) compared to the center. For a Gaussian beam with $1/e^2$-beam width w_a at the lens-plane, the field distribution is $E_g(r) = E_o \exp(-(r/w_a)^2)$. So, the edge taper for a lens radius a, is given by [41]:

$$TE(dB) = 10 \log \frac{|E_g(0)|^2}{|E_g(a)|^2} = 10 \log[\exp(2(a/w_a)^2)]. \qquad (2.10)$$

Aperture efficiency defines how efficiently an aperture couples Gaussian modes to a plane wave. The plane wave at the aperture or the lens-plane, E_{ap} can be written as a superposition of Gaussian modes as:

$$
\begin{aligned}
E_{ap}(x, y) &= \sum_{m=0}^{\infty} \sum_{n=0}^{\infty} A_{m,n} |\psi_m(\sqrt{2}x/w_a) \cdot \psi_n(\sqrt{2}y/w_a)\rangle \\
&= \sum_{m,n}^{\infty} A_{m,n} |G_{m,n}(\sqrt{2}x/w_a, \sqrt{2}y/w_a)\rangle, \qquad (2.11)
\end{aligned}
$$

where $\psi_m(\xi) = H_m(\xi) \exp(-\xi^2/2)$ is the m-th order Hermite-Gaussian mode [42], and $A_{m,n}$ is its excitation coefficient. The aperture efficiency for the (m.n)-th mode is given by [38]:

$$
\begin{aligned}
AE_{m,n} &= \frac{|A_{m,n}|^2 \langle G_{m,n}, G_{m,n}\rangle / 2Z_o}{\langle E_{ap}, E_{ap}\rangle / 2Z_o} \\
&= \frac{|\int \int_{aperture} E_{ap} G_{m,n} dxdy|^2}{\langle G_{m,n}, G_{m,n}\rangle \cdot \langle E_{ap}, E_{ap}\rangle}, \qquad (2.12)
\end{aligned}
$$

where Z_o is the free space wave impedance. After simplification, we find the aperture

30

efficiency of the fundamental Gaussian mode for a Gaussian lens antenna system is:

$$AE_{0,0} = 2(w_a/a)^2(1 - \exp(-(a/w_a)^2))^2. \tag{2.13}$$

The plots of Eq. 2.10 and 2.13 are shown in Fig. 2-9.

For the optimum aperture efficiency, $a/w_a = 1.12$ which corresponds to an edge taper of 11 dB. For higher edge taper, most of the power of the Gaussian beam is concentrated more towards the center of the lens or the radiating aperture. In a high edge taper system, the radiating aperture is not used efficiently, and it has a low aperture efficiency. It also produces radiation patterns with lower sidelobes and broader mainlobe. In a low edge taper system, radiation power is more uniformly distributed at the radiating aperture, and it has a high aperture efficiency. But the penalty is paid in terms of higher sidelobe levels. The choice of a particular edge taper or aperture efficiency depends completely on the desired applications. For our imaging array, we would like to couple plane waves to the fundamental Gaussian mode; so, we need to optimize the aperture efficiency. On the other hand, for an imaging system that radiates well-collimated Gaussian beams, it is undesirable to have a severe truncation of the propagating Gaussian beams [43]; so, a high edge-taper system will be more appropriate for it.

The maximum aperture efficiency for Gaussian beam optics antenna is 0.8. To produce a higher aperture efficiency, a hybrid field distribution is required [44]. For our 3×3 micromachined imaging array, we use a 175 mm diameter and 1.1 f-number (f/D) aspherical lens. The beam waist at the focal plane is set by the flare angle of the machined horn. Using a beam waist $w_0 = 3.1$ mm at the focal plane, and including the on- and off-axis feeds, we find an edge taper $\simeq 13.6$ dB and an aperture efficiency of $\sim 80\%$ for our lens-antenna system.

A given edge taper condition can also be analyzed in a different way. Edge taper defines how a gaussian beam is truncated by the focusing or radiating elements. For lower edge taper, the beam is truncated severely and the focused beam is no longer completely Gaussian. It contains sidelobes due to the effect of truncation. A good
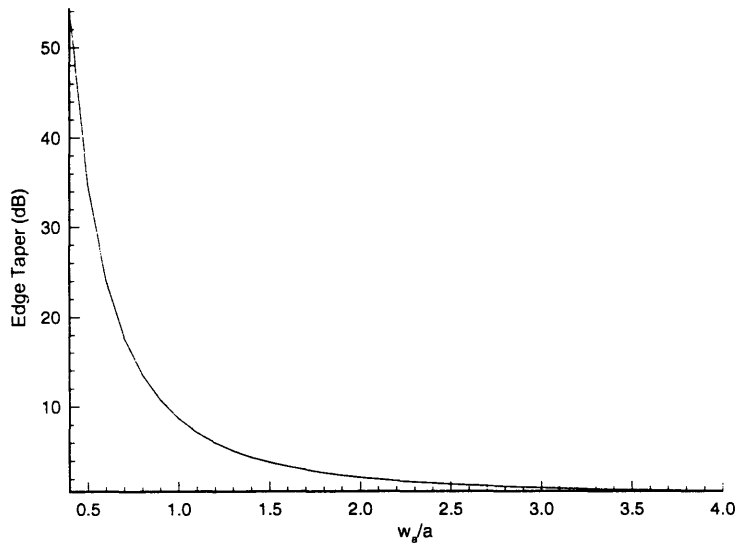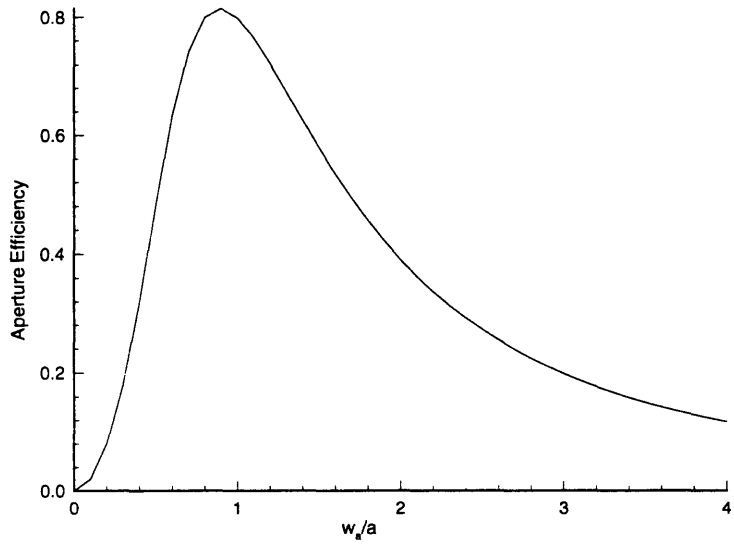
Figure 2-9: Plots for the aperture efficiency and the edge taper vs. normalized beam width at the lens-plane for a Gaussian lens antenna system.

design rule to reduce the effect of truncation is to use a lens or parabolic dish with diameter D such that $D \geq 3.5w_a$ [41, 45], where w_a is the beam width at the plane of the radiating aperture. In this case, the sidelobe levels are below 35 dB from the mainlobe.

2.4.2 Spacing of the Array Elements

In a focal plane imaging array, each receiver/detector images a different point of the target or a scene. The detectors should be placed close enough so that the sampled image at the focal plane can be reconstructed by doing some signal processing. Due to the diffraction of an image, the detected signal will contain information with spatial frequency less than a cutoff frequency f_c. In this respect, an optical system acts like a low pass filter with a diffraction-limited cutoff frequency. We can use the Nyquist's sampling theorem to find out the sampling intervals required to reconstruct the bandwidth-limited image. The Nyquist criteria is satisfied, if we sample at a rate $2f_c$. The sampled image can be represented as [21]:

$$g(x) = \sum_{n=0}^{\infty} g(n/2f_c) \cdot sinc[2f_c(x - n/2f_c)], \qquad (2.14)$$

where $g(x)$ is the image and $g(n/2f_c)$ is the electric field or intensity at the sampled points which are separated by $1/2f_c$. The cutoff frequency of an optical system is given by [21]:

$$f_c = n_1 \cdot (1/f{-}number) \cdot (1/\lambda), \qquad (2.15)$$

where n_1 is the index of refraction of the medium in which the image is formed, λ is the wavelength of interest. So the sampling interval to reconstruct the diffraction limited image is:

$$T_E = 1/2f_c = \lambda/n_1 \cdot f{-}number \qquad \text{for field detection}$$

and

$T_E = 1/4f_c = \lambda/2n_1 \cdot f\text{-}number$ for intensity detection.

We can also derive the required sampling interval (or the separation of the array elements) for a particular angular cross-over level between neighboring beams using Gaussian and ray optics formulas. Consider the Fig. 2-10 for a F/1 system, where there is a -3 dB cross-over level between the neighboring beams. For this configuration, by using Gaussian optics formulas [44], we get $\theta_{3\ dB} = 0.6\theta_{1/e^2}$, and
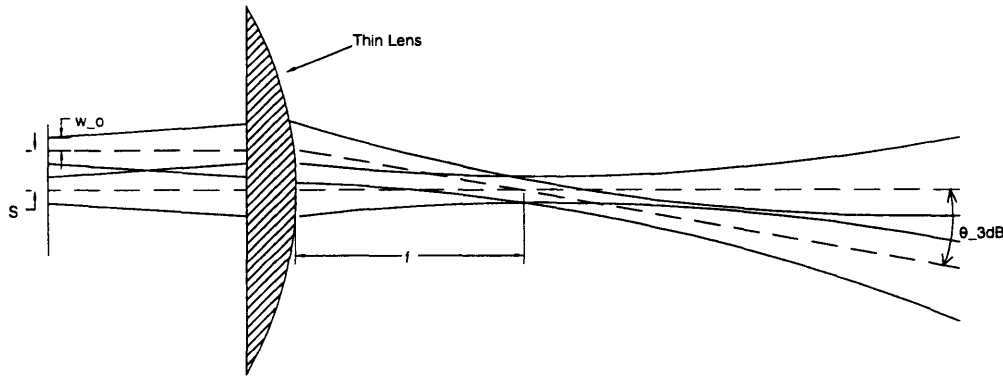
Figure 2-10: 3 dB beam widths of an on- and of-axis Gaussian beams as a function of distance from the focal plane. There is a -3 dB angular cross over level between these adjacent beams.

$\theta_{1/e^2} = w_0/f$, where θ_{1/e^2}, $\theta_{3\ dB}$ and w_0 are the $1/e^2$ and 3 dB beam divergence angles, and the beam waist at the focal plane, respectively. Also, $\theta_{3\ dB} \simeq s/f$, where s is the separation of the array elements, and f is the focal length. Using these values, we get an array element separation $s \simeq 1.12w_0 \simeq 1.12\lambda$. This is larger than the required array element separation calculated from the diffraction limited imaging theory. Yngvesson et al [46] has calculated the array element separations for various types of feeds for a $f/D = 1$ system, and for the maximum aperture efficiency they are between $\lambda - 1.15\lambda$. The separation of array elements for a slot-antenna imaging array presented in Ref. [43] is 1.15λ for the optimum aperture efficiency. In general, diffraction limited sampling does not always guaranty a high aperture efficiency, and

most of the imaging systems with high aperture efficiencies tend to undersample at the focal plane [43, 46].

In our micromachined mm-wave imaging array, the minimum separation between the array elements are set by the aperture size of the machined section, and it is $\simeq 3.5\lambda$. So, we undersample the image at the focal plane. This can be avoided by using a lens with a higher f-number. In this case, the Gaussian beams have to propagate a longer distance before they reach the lens plane. As a result, their beam widths will be greater, and they will be truncated severely by the lens. There will be a large spill-over loss due to the truncation. For our application, this is not desirable. So, we will use a F/1.1 lens and undersample at the focal plane. The $1/e^2$-beamwidths of the horn-array as a function of distance from the focal plane for array element separation of 3.5λ and 1.2λ are shown in Fig. 2-11.

It is apparent from Fig. 2-11 that for the 3.5λ separation, we undersample the image at the focal plane. In other words, there are "blind" spots at the scene that are not observable by any element in the array.

Yngvesson *et at* [40] has plotted the maximum number of array elements for -1 dB aperture efficiency loss due to off-axis aberration as a function of the f-number of the system. It has been assumed that the neighboring Gaussian beams have a -3 dB angular cross-over level. For a F/1 system, maximum number of array elements is $\simeq 11 \times 11$. Based on this calculation, and also considering the fact that the off-axis displacement of the array elements (13 mm) is much smaller than the focal length (175 mm), it is reasonable to assume that the off axis aberration of our imaging system is negligible.

35
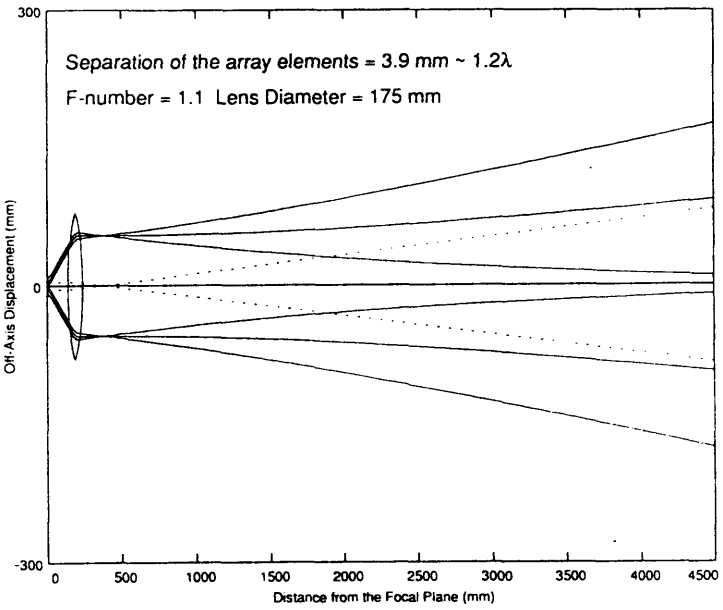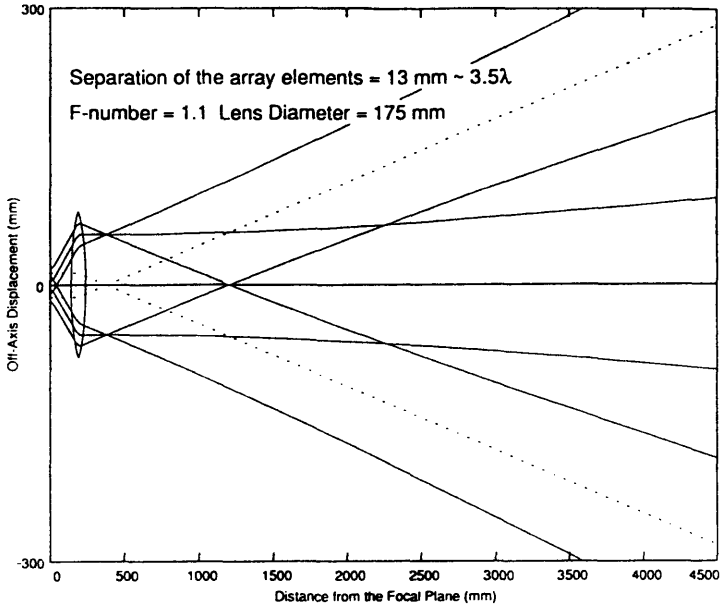
Figure 2-11: $1/e^2$-beamwidths of a Gaussian lens antenna system for two different separations of array elements. These results are calculated by using the Gaussian beam and ray optics formulas [44].

2.5 Summary

In this chapter backgrounds for the design and implementation of a microbolometer imaging array are presented. The importance of good radiation coupling structures, and how they influence the performance of imaging arrays are also addressed. A brief discussion on the microbolometer theory is provided that can be very useful for optimizing the sensitivities of the microbolometers.

Chapter 3

Microbolometer Design and Fabrication

The fabrication process of the micromachined Nb microbolometers is simple and compatible with the integrated circuit (IC) device fabrication process. They can be fabricated easily by using standard photolithographic techniques. In this chapter, first, a brief discussion on the micromachined microbolometer design and the mask layout will be given in section 3.1 and 3.2, respectively. Then all the device fabrication steps will be summarized in section 3.3. They include pattern definition of the Nb strips, infrared (IR) alignment, antenna metallization and the anisotropic KOH etching to form the pyramidal cavity. Some of these fabrication steps are similar to the SIS-fabrication steps, but they are much simpler than those of the SIS.

All the devices used in this project are fabricated in the clean room of group 86 of Lincoln Laboratory. For the Nb microbolometer fabrication, we use double side polished 4-inch, (100) Si wafers which are purchased from the Virginia Semiconductor [47]. The resistivity of the device wafers is greater than 2000 $\Omega-cm$, and for the aperture wafers it is 1000 $\Omega-cm$. These wafers are sent to the Center for Integrated System (CIS) at the Standford University [48] for low stress LPCVD Si_3N_4 deposition on both sides of the wafers. Currently, all the wafers that have been processed for the Nb microbolometers had $1-\mu m$ thick Si_3N_4 deposited on them, but in future, we would like to have a $0.5-\mu m$ thick Si_3N_4 deposited on both sides of the Si wafers. For

a thinner Si_3N_4 membrane, the microbolometer will have a higher thermal isolation, and as a result, its sensitivity will be better. Next, these 4-inch round wafers are coated with photoresist FSCM [49] and diced to 2-inch and 3-inch diagonal squares for the 195 GHz and 95 GHz microbolometer fabrication, respectively. The design and fabrication process of the micromachined Nb microbolometers will be presented in the following subsections.

3.1 Microbolometer Design

Some of the important design issues for a good microbolometer are:

a) provide good thermal isolation to the microbolometer,

b) optimize the coupling efficiency by choosing the appropriate radiation coupling structure,

c) and use a simple and inexpensive device fabrication process which is compatible with the IC device fabrication techniques.

Thermal isolation to the micromachined microbolometer is provided by fabricating it on a $1-\mu m$ thick Si_3N_4 membrane, and the coupling efficiency is enhanced by using a micromachined horn structure [10]. Thermal isolation can be increased further by etching away Si_3N_4 membrane not directly below the dipole antenna and the micorbolometer. The coupling efficiency can also be optimized by using a corrugated or conical horn. These design ideas are currently pursued in our group for the next generation micromachined microbolometers and the SIS devices.

The schematic of the microbolometer and the dipole antenna is shown in Fig. 2-1. The Nb strip that acts as a radiation absorber and temperature sensor has typical dimensions of 2 μm × 3.2 μm. However, in the new set of devices, we use microbolometers with four different aspect ratios, and they are 5 μm long and 1, 2, 3 and 4 μm wide. The thickness of the Nb film is 20 nm, and the resistance of the microbolometer is in the range of 20 Ω − 45 Ω. The dipole antenna and the coplanar
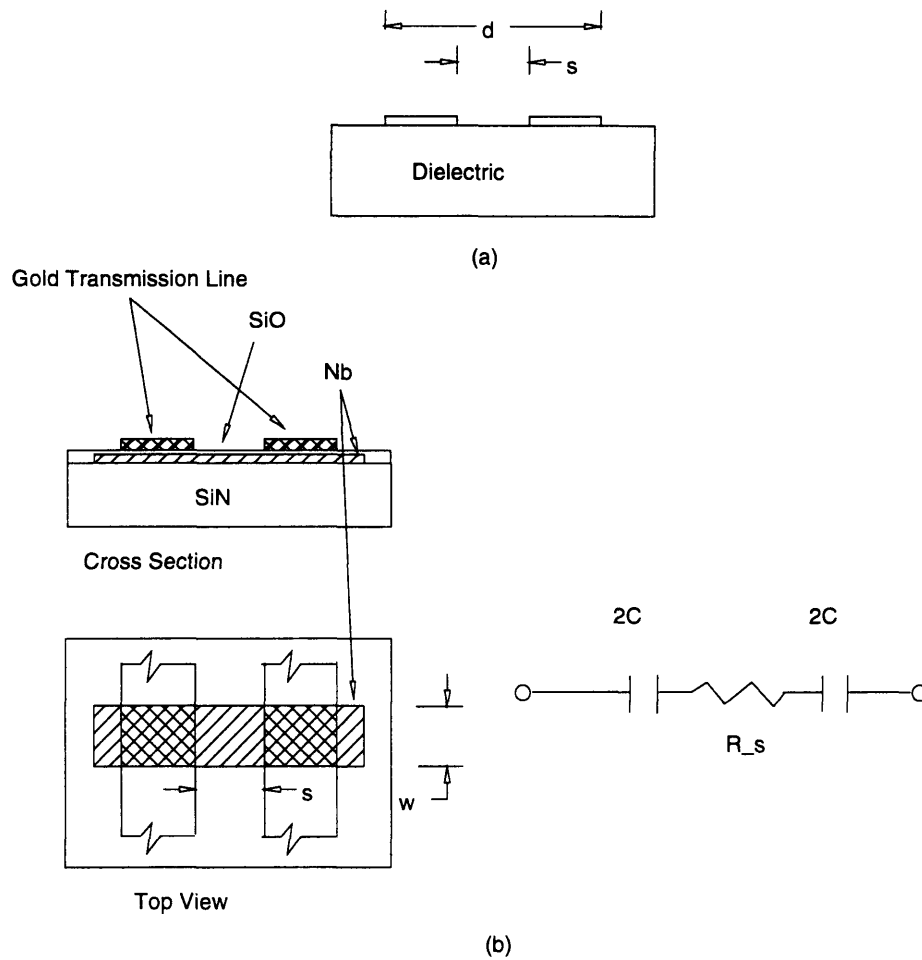
Figure 3-1: (a) Cross section of a coplanar transmission line. (b) RF choke capacitor and its equivalent circuit model. In this figure, s=10 μm and w=15 μm. The series resistance R_s is in the range of 15 Ω-20 Ω and the total capacitance is $\simeq$ 270 fF.

transmission line are formed by a 20$-nm$ titanium and a 200$-nm$ gold films. The DC bias to the microbolometer is provided through the coplanar transmission line. and it has a DC resistance of $\simeq$ 30 Ω.

The radio frequency (RF) choke capacitor is used to block the RF from propagating through the coplanar transmission line. It electrically shorts the transmission line at high frequencies, and this short circuit is transformed into an open circuit at the dipole antenna terminals by the quarter-wave transmission line. So, the RF encounters a large impedance and cannot propagate through the transmission line.

The characteristic impedance of the coplanar transmission line (shown in Fig. 3-1(a)) can be calculated from the following formulas [50]:

$$Z_0 = \frac{\eta_0}{\pi\sqrt{\varepsilon_{r,eff}}}[\ln 2 + 2\tanh^{-1}\sqrt{s/d}] \qquad for\ 0.137 \le s/d$$
$$= \frac{\pi\eta_0}{4\sqrt{\varepsilon_{r,eff}}\ln(2\sqrt{d/s})} \qquad for\ 0.137 \ge s/d. \qquad (3.1)$$

s and d are shown in Fig. 3-1(a), and $\varepsilon_{r,eff} = (\varepsilon_r + 1)/2$. For the quarter-wavelength section, $\varepsilon_{r,eff} \simeq 1$ because the the transmission line is essentially standing freely on air. Using $s = 10\ \mu m$ and $d = 50\ \mu m$, we get an impedance of 184 Ω for the quarter-wave transmission line. Similarly, for the coplanar transmission line that lies on the Si wafer, the impedance is 43 Ω, where we have used $\varepsilon_{r,eff} = \varepsilon_{Si} = 11.8$, $s = 10\ \mu m$ and $d = 140\ \mu m$. The RF choke capacitor is formed by sandwitching a $200-nm$ thick layer of SiO between a Nb strip and the gold transmission line (as shown in Fig. 3-1(b)), and it has a capacitance $C \simeq 270\ fF$. Due to the finite resistance of the Nb film at 300 K, there will be a series resistance (15 Ω – 20 Ω) added to the RF choke capacitor. The impedance seen by the dipole antenna Z_{in} can be found by transforming the impedance of the RF choke capacitor at the dipole terminal by using the well known formula [51]:

$$Z_{in} = Z_{\lambda/4} \cdot \frac{Z_L\cos\beta l + jZ_{\lambda/4}\sin\beta l}{Z_{\lambda/4}\cos\beta l + jZ_L\sin\beta l}, \qquad (3.2)$$

where $\beta l = \pi/2$ for the quarter wave transmission line, $Z_{\lambda/4} = 184\ \Omega$ and $Z_L = R_s + 1/j2\pi fC$. For the worst case, with $R_s = 20\ \Omega$, we get a $-11\ dB$ optical coupling loss due to the RF transmission through the coplanar transmission line.

Another source of coupling loss may arise from the mismatch of impedance between the microbolometer and the dipole antenna. The impedance of the dipole antenna is 35 Ω, and the microbolometer's resistance is 20 Ω – 45 Ω. In the worst case, this corresponds to a RF reflection loss of $-12\ dB$. Typical aperture efficiency of the micromachined horn antenna is $\simeq 90\%$ [6]. If we take into account all the

41

losses, we get an overall optical coupling efficiency of $\simeq$ 80% for the micromachined microbolometer.

3.2   Mask Layout

Brian Jacobson generated the drawing files using KIC, a mask-layout software available in our microsystem technology laboratory (MTL) account. KIC is not a very user friendly program, and many companies don't accept KIC files. I used Autocad to generate the drawing files. However, if the masks are being made at the MTL, there is no choice but to use KIC because they don't accept Autocad files. The companies that accept the Autocad files, generally convert them to a different format (MEBES) which is used for mask generation. The mask manufacturers have some guidelines for the Autocad drawing files. So, it is recommended that first, these guidelines should be obtained, and all the drawings should comply with them. I have used BLOCKs [52] to generate the Autocad drawing files. A BLOCK is a drawing file that can be inserted into other drawing files or BLOCKs. It plays the same role in Autocad drawings, the way a subroutine or a function does in a computer code/program. If a BLOCK is inserted multiple times on a drawing file, Autocad stores only the address of the location where it is inserted rather than storing the BLOCK definition multiple times. Thus, one can reduce the size of the data files significantly by using BLOCKs. All the Autocad drawing files (in *.DXF format) are sent to Photronics [53] for mask generation.

3.3   Device Fabrication

The first step after obtaining the diced wafers is to strip the protoresist (PR) off them and go through a standard cleaning step. The wafers are cleaned in acetone for 5 minutes, in methanol for another 5 minutes and then rinsed in distilled water. If there is any grease in the wafers, first, they should be stripped off the PR and then cleaned in tricloroethalene (TCE) at 70° C to remove the grease. Next, they

are plasma ashed for 1 *min.* to remove organic residues from the wafers and then placed in vapor HMDS (hexamethyleclisilizane) for 10 *min.* Vapor HMDS removes the water molecules from the wafers so that the photoresist can stick to the wafer surface more efficiently.

In the second batch of device fabrication, we wanted to fabricate the microbolometers on a $0.5-\mu m$ Si_3N_4 membrane, but we had Si wafers that were covered with only $1-\mu m$ Si_3N_4. So, before the Nb film deposition, the Si_3N_4 membrane is thinned down to 0.5 μm by reactive ion etching (RIE). The RIE etcher has a very undesirable characteristic because it etches more at the center of the wafer than the edges, and according to Earle Macedo the nonuniform etch rate can be as large as 25%. This nonuniformity is more pronounced in the 3-inch wafers than the 2-inch wafers. I thinned the Si_3N_4 membrane in half of the total number of wafers that I processed to 0.5 μm, and the other half had a $1-\mu m$ Si_3N_4 membrane.

3.3.1   Nb Film Deposition and the Microbolometer's Pattern Definition

The Nb film is deposited on the device wafers by DC magnetron sputtering at a base pressure of 5.6×10^{-7} $Torr$ and at a rate of 24 $\mathring{A}/sec$. Typical measured and theoretical Nb film resistances for various film thicknesses are given in Table 3.1. The theoretical values are based on the properties of the bulk Nb [13]. I have found that the measured film resistance varied 20% − 35% for Nb films that were deposited at various times.

Film Thickness (nm)	Theory ($\Omega/\square$)	Measured ($\Omega/\square$)
10	14.5	34.6
20	7.25	12.1
30	4.8	7.7

Table 3.1: Measured and theoretical Nb film resistance for various film thickness. Theoretical values are calculated using the bulk resistivity of 14.5 $\mu\Omega \cdot cm$ [13]. The measurement accuracy is ± 2 Ω.

The Nb film resistance as a function of temperature is measured at the group

43
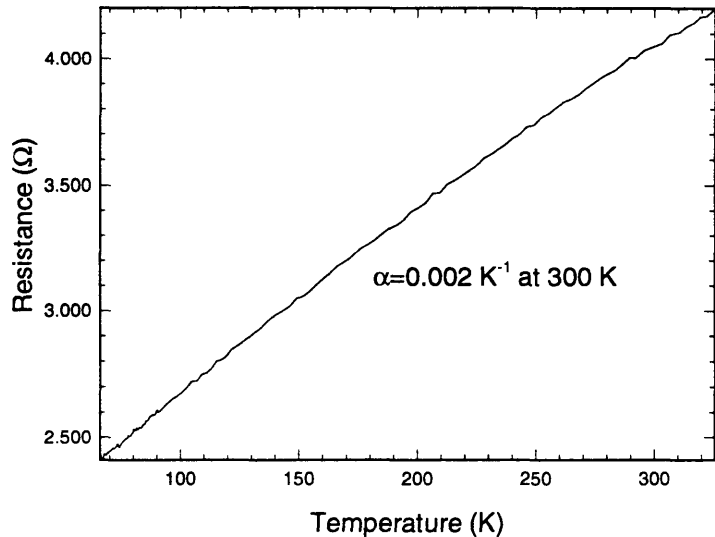
Figure 3-2: R vs. T plot of a 20-nm Nb film deposited on a Si wafer covered with $1-\mu m$ Si_3N_4. The measured temperature coefficient of resistivity generally lies between $0.001 - 0.002$ K^{-1}.

86's measurement and test facility with the help of Rene Boisvert. A four-point measurement setup is used for this purpose. The temperature range can be varied from 4 K $-$ 350 K. To fit the test wafers on the sample holder, they must be ≤ 1 cm $\times 1$ cm. A typical R vs. T. plot of a Nb film is shown in Fig. 3-2.

The next step is to pattern the Nb microbolometer by defining the device geometry with PR and then by etching away the Nb films not covered with the PR by plasma or RIE etching. If the microbolometer definition in the mask is in crome, a positive photoresist like 1470 or 4620 from Shipley [49] is used to define the Nb strip. Otherwise, if it is clear field, an image reverse or negative resist like AZ-5218 or AZ-5214 from Shipley [49] should be used. Areas on the Si wafer that are under the crome areas of the mask are not exposed to the ultraviolet (UV) rays. After developing the wafers that have been processed with a positive photoresist, the PR is stripped off the areas that have been exposed to the UV rays. The opposite is true for the wafers processed with a negative PR.

When we pattern the Nb strips, we also pattern some alignment marks that are
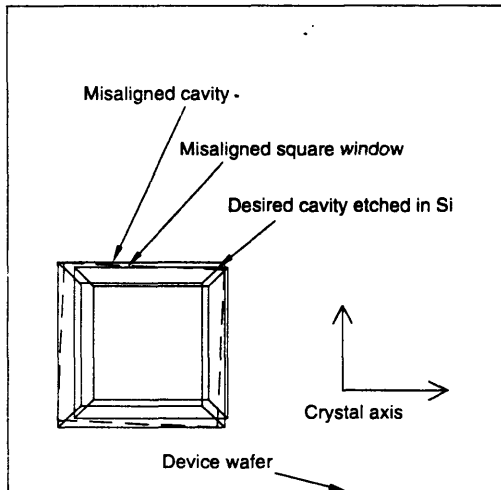
Figure 3-3: This figure shows the effect of misalignment of the square windows with the crystal axis. This effect will be more pronounced for an array of windows, where all of them must be aligned to the crystal axis.

used later for infrared alignment. The square windows that we pattern by IR alignment must be aligned to the crystal axis. Otherwise, the KOH etching will form cavities, etched in silicon, with different dimensions than desired because the cavity-sizes are determined by the largest dimensions of the windows (etched in Si_3N_4) along the Si-crystal axis. This is illustrated in Fig. 3.3.1, where due to misalignment of the square window etched in Si_3N_4, the cavity formed after KOH etching is larger than the originally designed cavity. To ensure correct alignment, the boarder lines of the mask are aligned to the crystal axis. This also aligns all the alignment marks, and eventually, the square windows to the crystal axis.

Nb film can be etched away from the areas that are not covered with the photoresist by plasma or RIE etching. The plasma etcher works better and is preferred over the RIE etcher because it etches more uniformly than the RIE etcher. Moreover, the plasma etcher does not attack the Si_3N_4 membrane aggressively like the RIE etcher. In the plasma etcher, a heat-plate heats up the chamber to 70^0 C so that the etched Nb which is the form of niobium floride gas becomes more volatile, and it is easily removed from the chamber. During my second batch of device fabrication, this heat plate was not working. So, I had to etch at room temperature, and I noticed that some of the etched Nb film was redeposited on the device wafers. I didn't want to risk destroying them and decided to use the RIE etcher.

The Nb etch rate in the RIE etcher for a plasma created by 6 sccm argon and 14

sccm freon at a base pressure of 20 mTorr, and RF power 60 Watt is 1353 $\mathring{A}/min$. Taking into account the nonuniform RIE etch rate, the time required to etch the $20-nm$ thick Nb film is 12 s − 16 s. However, the RIE etcher gets very hot during the etching process, and the PR may crack due to excessive heating. So, we etch the Nb film in two steps, each 6 $sec.$ − 8 $sec.$ long, and in between these steps we cool down the chamber for 10 minutes. After the Nb etching, the wafers are prepared for the IR alignment.

3.3.2   Infrared Alignment

Infrared alignment is needed to pattern square windows on the back side of the device wafer. We etch away Si_3N_4 from these square windows so that the Si wafer is exposed to the anisotropic wet etch, KOH solution through these square windows. The IR alignment is performed in group 84's Si-fabrication lab. They don't like gold in their system because it is a contaminant in Si-processing. So, the IR alignment is performed before the gold deposition to define the dipole antennas. Group 84's mask aligner operate at a different UV wavelength than the one in group 86's clean room. So, the appropriate exposure time must be obtained for processing the device wafers. The KOH etching is performed at the end of the fabrication process after the antenna metallization.

We protect the device side of the wafer during IR alignment by placing it on a backing wafer. First, the backing wafer is coated with photoresist FSCM. and then we place the device wafer (device side facing FSCM) on top of the backing wafer. Now they are baked at 100^0 C for one minute. FSCM glues the two wafers together well enough so that we can spin PR on the back side of the device wafer. One critical thing to note is that the backing wafers should be double-side polished. Otherwise, the IR is scattered significantly due to the surface roughness, and it is almost impossible to align the alignment marks on the device wafer with those of the mask. To have a significant transmission of IR through the Si wafer, the backing wafers should be 10 mil − 15 mil thick. I have also tried the IR alignment without using a backing wafer. In this case, the device side is covered with FSCM, and all other processing
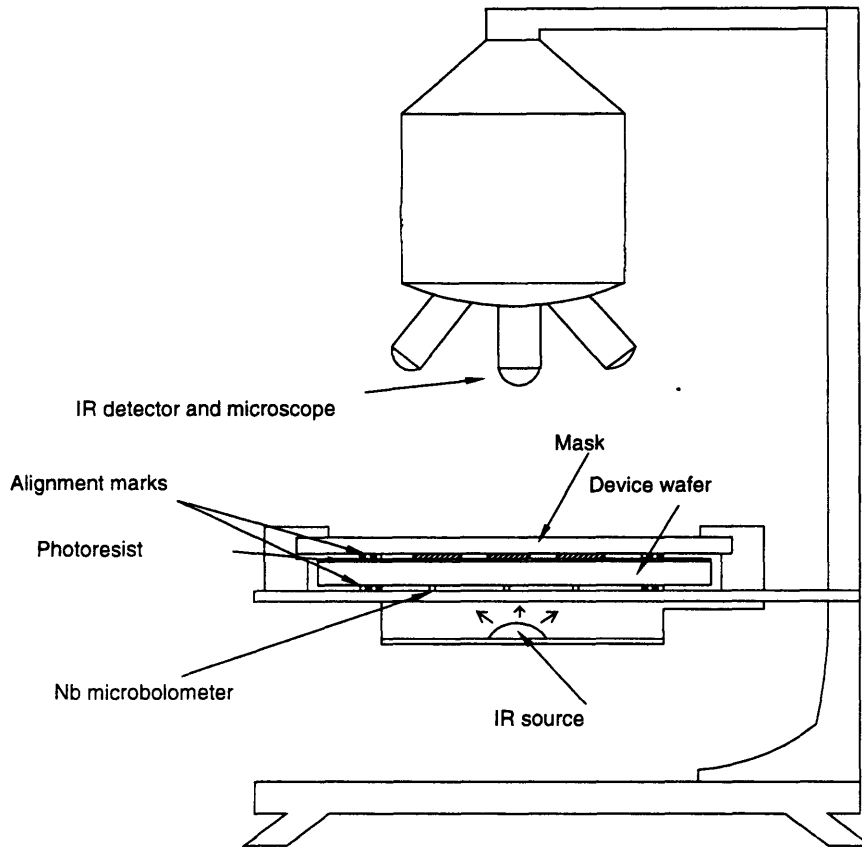
Figure 3-4: IR aligner setup for patterning square windows on the back side of the device wafers. For illustration purposes, the sizes of the mask and the device wafer are exagerated.

steps remain the same. The IR alignment without a backing wafer is much easier than with the backing wafer. Also, I have not noticed anything unusual when the backing wafer is not used for the IR alignment. A schematic of the IR aligner setup, without using a backing wafer, is shown in Fig. 3.3.2.

After defining the square windows by IR alignment, we etch away the Si_3N_4 by RIE etching. When the square windows are defined by IR alignment, other unwanted structures from the mask could also be defined on the device wafer. Before placing the device wafer on the RIE etcher, we paint these unwanted structures with photoresist so that Si_3N_4 will not be etched from these areas. If they are RIE-etched and lie underneath the o-ring of the KOH mount, KOH will etch through these structures, and the o-ring will not be effective in preventing the KOH solution from attacking
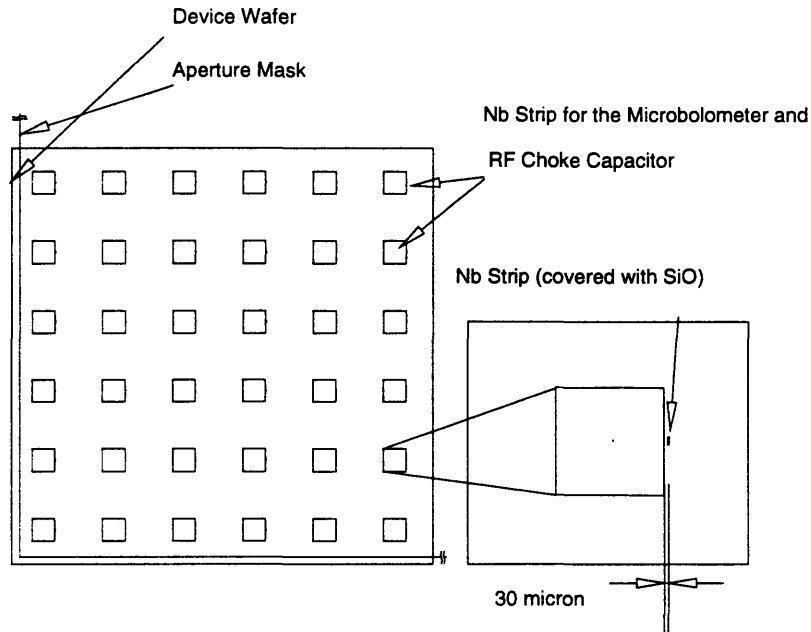
Figure 3-5: This figure shows how the aperture mask for the device wafer is used to pattern the areas for the *SiO* deposition. If the aperture mask is not shifted, the Nb strips that form the RF choke capacitor lie inside the square windows.

the Nb films. We remove the RIE-mounting grease from the device wafer by TCE. If a backing wafer is used, the wafers are kept in acetone for 1 − 1.5 hour to separate them. Then they are cleaned in methanol and distilled water.

3.3.3   SiO Deposition and the Gold Antenna Metallization

The dielectric used to form the RF choke capacitors is a $200-nm$ thick *SiO*. No additional mask is needed to define the areas for *SiO* deposition; the aperture mask for the device wafer is used for this purpose. We shift the aperture mask so that there is a 20 μm − 30 μm separation between an edge of the square windows and the Nb strip (as shown in Fig. 3-5). *SiO* is deposited everywhere and then lifted off the square windows. For lift-off, the PR must form overcut or vertical side walls (see Fig. 3.3.3). Among the PR available in the Lincoln Lab., photoresist 1470 creates vertical side walls, and AZ-5218 creates overcut profiles. I was not able to obtain consistent results with the PR 1470; so, I used AZ-5218 for the *SiO* lift-off.

48

Photoresist Profile	Application
Vertical | Dry Etch, Wet Etch

Lift-off |
|
Overcut | Ion Implant

Lift-off |
|
Undercut | Dry Etch, Wet Etch |
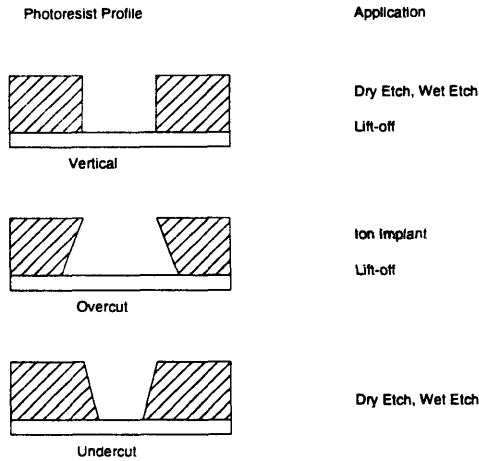
Figure 3-6: Side wall profiles created by different types of photoresis. Phoresists 1470 and AZ-5218 create vertical and overcut profiles, respectively. For lift-off, a rule of thumb is to use a PR thickness three times the thickness of the deposited film.

After the SiO deposition, the device wafer is sputter-cleaned, and the dipole antenna and the bias contact leads are defined by electron beam evaporation of a 10 nm titanium (used as an adhesion layer) and a 200 nm gold film, followed by a gold lift-off process. Niobium film has a tendency to form niobium oxides at the surface, and this oxide layer may prevent good ohmic contact with the Nb film. So, the sputter-cleaning step is very critical for making good gold contact with the Nb film. After the gold metallization, we measure the resistance of the microbolometer and the gold antenna at two or three different temperature to determine if the Nb microbolometer shows any unusual characteristic [10].

3.3.4 KOH Etching for the Aperture Fabrication

KOH is an anisotropic etchant that has an etch rate of $\langle 100 \rangle$ silicon aobut 400 times faster than that of $\langle 111 \rangle$ silicon [54]. The etch rate also depends on the concentration and the temperature of the KOH solution. The KOH etch rate as a function of its concentration and temperature can be found in Brian Jacobson's thesis [55]. We etch the device wafers in 20% KOH solution by weight at 80^0 C for about 4.5 hours and then at 60^0 C until the membrane is cleared of silicon. During the etching process, we protect the device side from the KOH solution by mounting it on a teflon mount.

A schematic of various types of KOH mounts shown in Fig. 3.3.4. An o-ring, pressed against the device wafer prevents the KOH from attacking the important
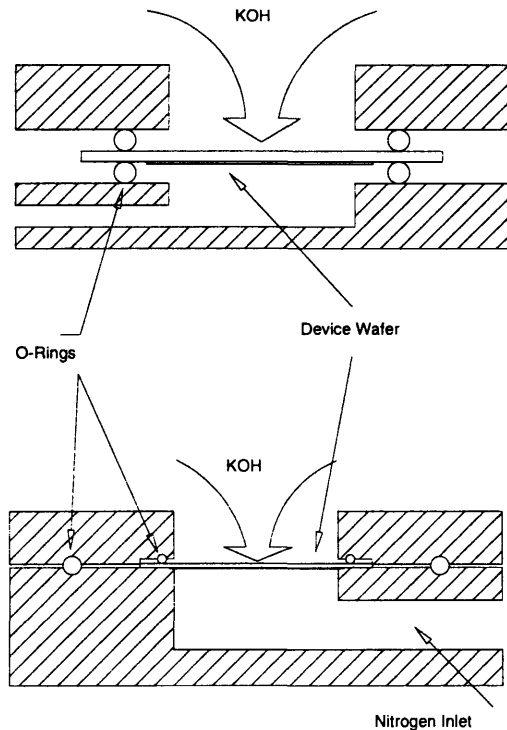
Figure 3-7: Various types of teflon mounts used for the anisotropic KOH etching.

areas of the device wafer. A 0.5-1 psi nigrogen gas is fed through a pipe to pressurize the areas underneath the wafer to prevent KOH coming through any pinholes in the silicon nitride membrane. A KOH solution autolevelling system [55] is used to keep the concentration of the KOH solution constant during the etching process.

In order to fabricate the microbolometer and the gold antenna on a '+'-shaped structure (shown in Fig. 3-8), we define the '+' with PR 1470 before placing the device wafer in the KOH mount. After the anisotropic KOH etching, the device is cleaned in distilled water, and the Si_3N_4 is etched away from the areas not covered with photoresist in the RIE etcher.

We do not need any KOH mount to etch the aperture wafers, and they are simply submerged in KOH. After the KOH etching, the Si_3N_4 is removed from them by RIE etching. We cover the side walls of the aperture wafers with gold in electron beam evaporator. For the device wafer, a laser-cut shadow mask is used to cover the membrane so that gold is evaporated only on the side walls of the aperture. Another shadow mask is used to cover a small part of the side wall on the aperture wafer that is placed underneath the device wafer. This covers area that is directly below the
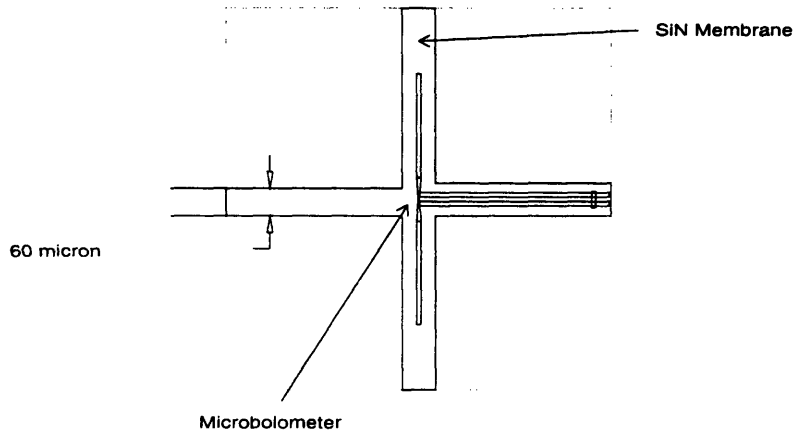
Figure 3-8: The +-shaped structure which can be fabricated by etching away Si_3N_4 membrane in the RIE etcher. The width of the cross is 60 μm, and it is 1600 μm long.

coplanar transmission line. We form the pyramidal cavity by stacking the aperture wafers under a microscope with an optical gule.

To make bias contacts with the gold antenna pads, we etch holes through the Si wafers by KOH etching. This is shown in Fig. 3-9. The contact is made with spring-loaded (pogo) pins, and these pogo pins are mounted on a PC board and connected to the bias circuits.

3.3.5 Machined Horn

The gold-plated machined horn section is placed in front of the micromachined section to reduce the flare-angle and improve the Gaussian beam coupling efficiency. The single machined horn section was ordered from the Custom Microwaves [56], and it was made by using a mandrel. For a 3×3 machined horn-array, they need 9 mandrels, and the total fabrication cost is very high. Recently, this type of machined horns have been fabricated by using split-block technique [57]. We apply this technique

51
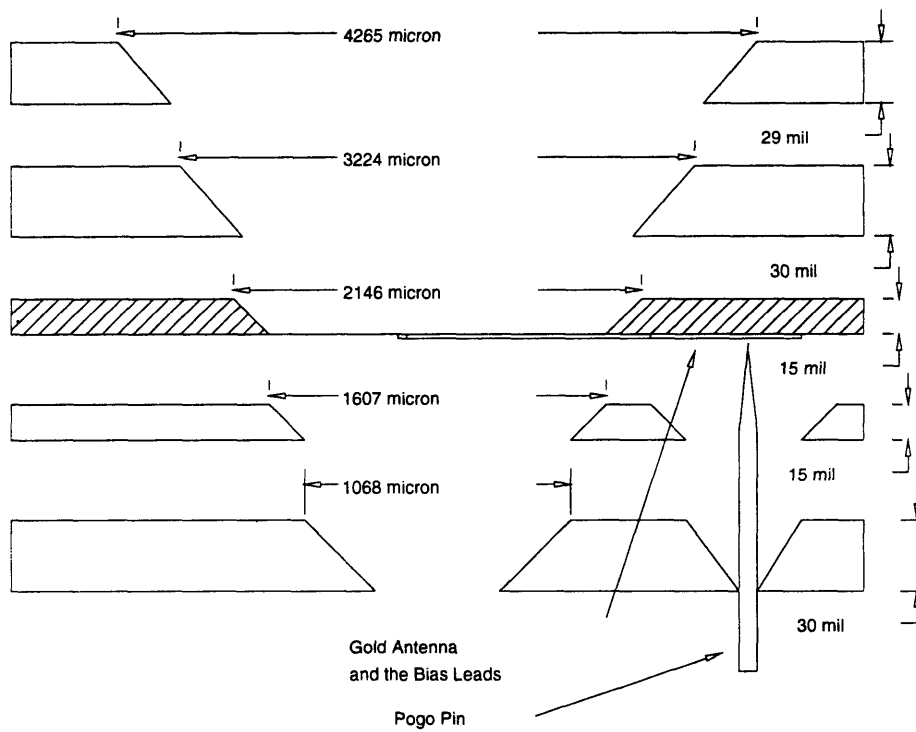
Figure 3-9: Micromachined pyramidal cavity for the 95 GHz Nb microbolometer. This feature is repeated 3×3 times on a 2-inch wafer for fabricating the micromachined horn-array. Holes are etched in the Si wafers underneath the device wafer by KOH etching to make the bias contacts with pogo pins.

to fabricate our 3 × 3 machined horn-array, and it is fabricated by Skip Williams in the machine shop of group 63, Lincoln Laboratory. A schematic of the machined horn-array is shown in Fig. 3-10.

In future, we would like to explore the possibilities of fabricating corrugated square and conical horns. Corrugated horns can launch very symmetrical beams, and they have small sidelobe levels [41]. Fabrication of this type of horns by stacking thin platelets have been reported in Ref. [58]. We can laser cut thin (5 mil − 10 mil) metal plates or Si-wafers, and then stack them to form these platelet-horns.

3.4 Summary

In this chapter the design and fabrication of the micromachined Nb microbolometer are presented. Some critical fabrication steps that may ruin the fabrication process if they are not followed properly are discussed. Future design considerations to optimize the performance of the microbolometers are also summarized.
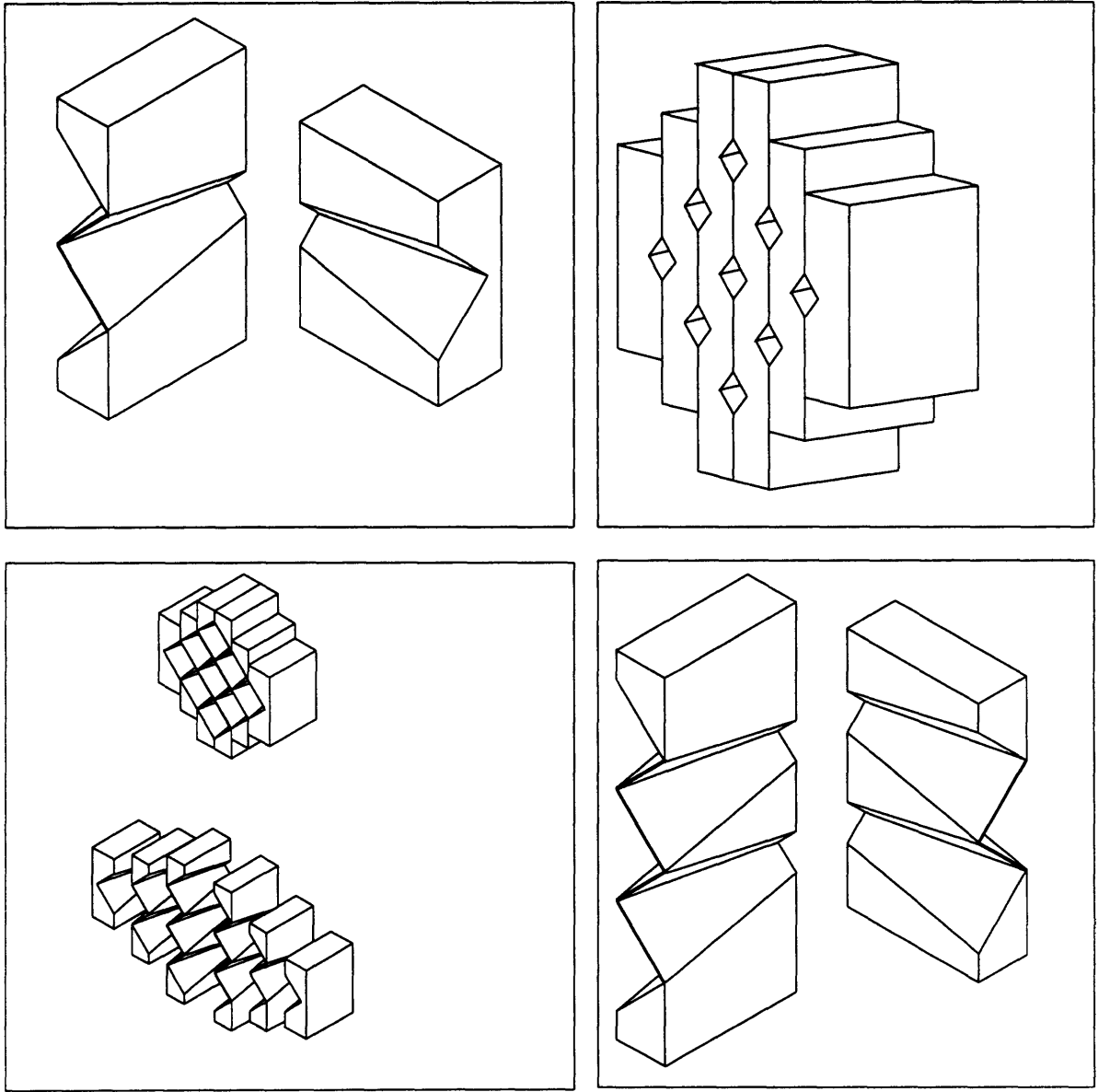
Figure 3-10: Schematic of the machined horn-array that has been fabricated by using the split-block technique.

Chapter 4

Experimental Results and Analyses

In this chapter. experimental results for the micromachined Nb microbolometer will be presented. A brief discussion on the measurement setup will also be given. First, in section 4.1. the DC measurements are summarized. We present the RF measurements in section 4.2. Finally, the experimental results on the electrical noise equivalent power of a micromachined Nb microbolometer are given in section 4.3. When this thesis was completed, experimental data for the focal plane imaging array was not available. So, the results that are presented in this Chapter are for a single micromachined Nb microbolometer.

4.1 DC Measurements

The DC measurements are performed systematically to characterize the microbolometer. In the original DC measurements we measure the voltage drop across the microbolometer and the antenna leads, but in the experimental results that are presented here, the voltage drop across the antenna leads (with a resistance of $\simeq$ 30 Ω) has been subtracted from the original data. A computer controlled measurement setup is used to measure the current (I) vs. voltage (V) and dV/dI vs. V characteristics. We deduce the voltage responsivity vs. bias voltage curve from the I-V plot by using the

Jone's expression which is given by [59]:

$$S_E = \frac{Z - R}{2IR},\qquad (4.1)$$

where $Z = dV/dI$ and R is the resistance of the microbolometer.

When I measured the I-V curve of the Nb microbolometer, I found something very unusual. The Nb microbolometer showed a semiconductor type of behavior; the resistance of the microbolometer decreased as more power was dissipated in it. This is evident clearly from the I-V and dV/dI vs. V plots shown in Fig. 4-1(a).

All the devices that I examined had similar characteristics. To probe further into this unusual finding, I measured the resistance of the microbolometer as a function of temperature, and the ln(R) vs. $T^{-1/2}$ curve showed a nonmetallic behavior, and it is shown in Fig. 4-2

How can we explain this? First of all, the I-V curve (Fig. 4-1(a)) is slightly asymmetric, suggesting that the ohmic contacts between the gold leads and the Nb film are not very good. In other words, there might be asymmetric barriers between them which can explain the asymmetry in the I-V curve. By measuring the I-V curve at 77 K and from the frequency response of the device (to be discussed later in this chapter), we concluded that the nonmetallic behavior is probably not due to the bad ohmic contacts between the gold leads and the Nb strip.

It is plausible to suspect that the original Nb film was transformed into a composite of Nb and niobium oxides during the fabrication process. Nb film has a tendency to form niobium oxides when left in air. Among all the niobium oxides, niobium monoxide (NbO) has an insulating characteristics [60]. But niobium pentaoxide (Nb_2O_5) being a binary compound might exhibit ranges of variable composition (nonschoichiometry) in a way similar to that exhibited by the III-V compound semiconductors [61]. For example, if the nonstoichiometry would lead to regions of variable composition in which a metal excess is present and Nb_2O_5 would behave as defects, the nonstoichiometric Nb_2O_5 might exhibit n-type semiconductor characteristics. Greener et al [61] presented experimental results which show an exponential dependence of
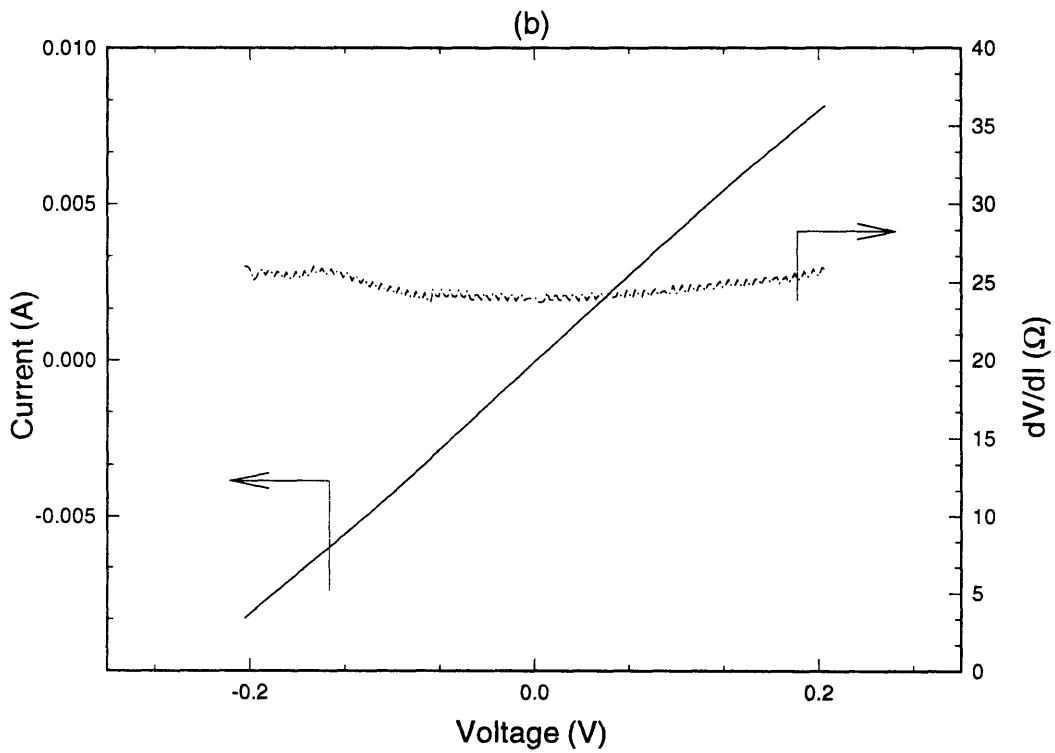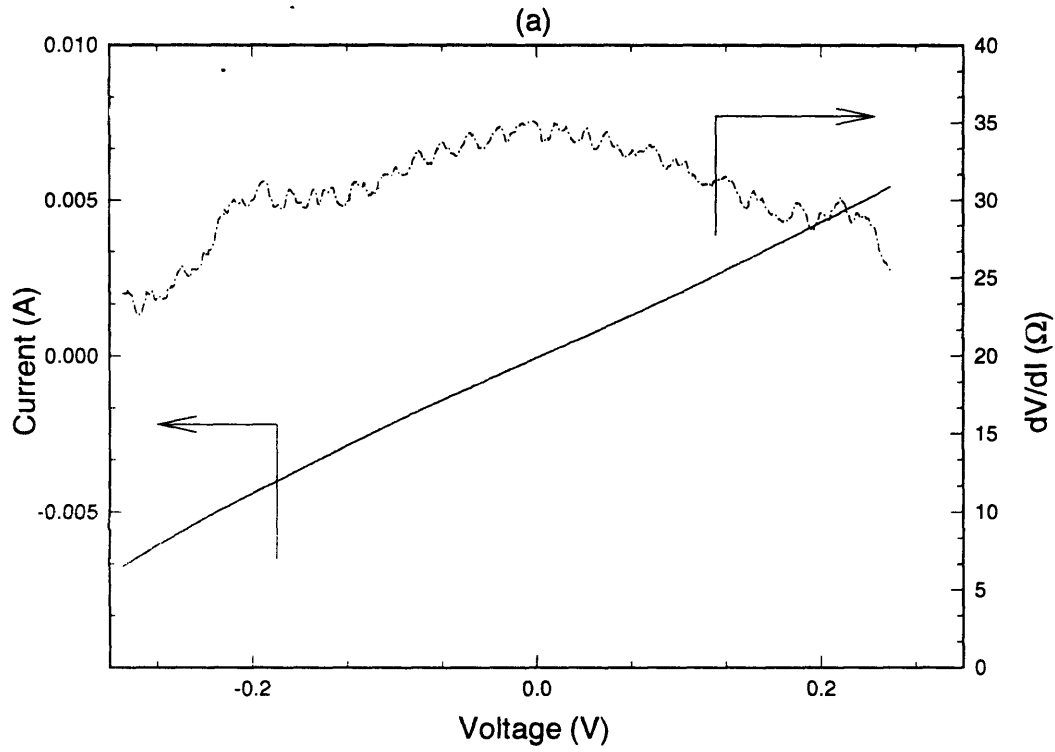
Figure 4-1: The I-V and dV/dI vs. V curves for a 10 nm Nb microbolometer (a) before and (b) after annealing. In (a), the differential resistance decreases as more power is dissipated on the device, where as in (b) it increases.
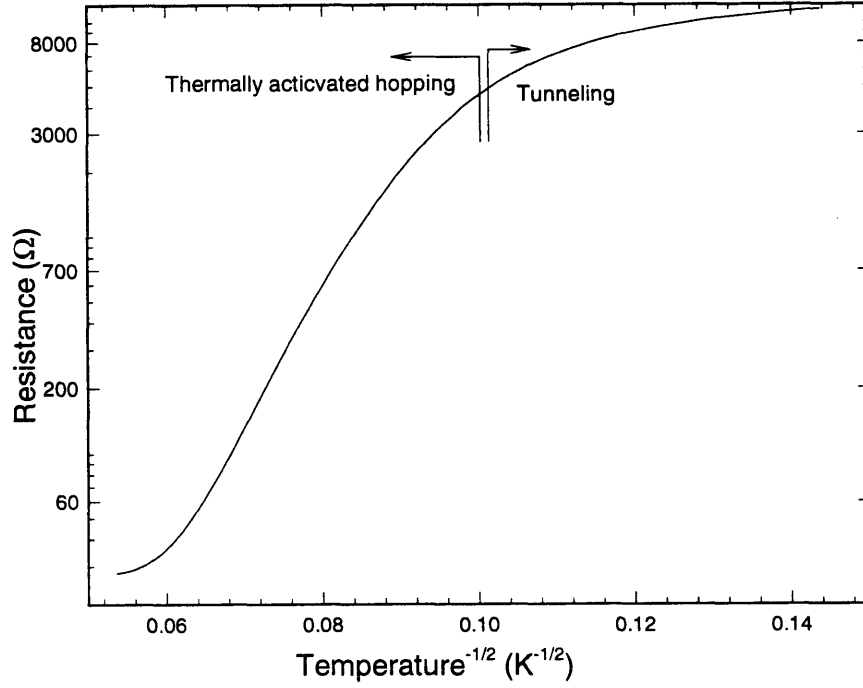
Figure 4-2: Resistance vs. (Temperature)$^{-1/2}$ of a 20-nm Nb microbolometer. In the range $0.055\ K^{-1/2} \leq T^{-1/2} \leq 0.1\ K^{-1/2}$ the R vs. $T^{-1/2}$ plot is approximately linear, and for $T^{-1/2} \geq 0.1\ K^{-1/2}$, it is weakly dependent on the temperature.

resistance with temperature for nonstoichiometric Nb_2O_5 film.

We may also expect a nonmetallic behavior if the conduction process is due to thermally activated hopping [62, 63]. For hopping conduction, electron in an occupied state with energy below the Fermi level receives energy from the phonons to move to an empty state above the Fermi level. This conduction process depends on the hopping distance and the activation energy required for hopping [62]. For hopping conduction, the resistance follows a temperature dependence given by:

$$R(T) = R_0 \exp(T_0/T)^{1/2} \qquad (4.2)$$

For a pure semiconductor film the resistance has an exponential dependence with $1/T$, and for hopping conduction, this exponential dependence is with $(1/T)^{1/2}$. So, from the $\ln(R)$ vs. $1/T$ or $1/T^{1/2}$ plot, we can determine which type of conduction process dominates in a particular material. If we examine Fig. 4-2, we find that in

the temperature region 100 $K \leq T \leq 300$ K, which corresponds to 0.055 $K^{-1/2} \leq$ $T^{-1/2} \leq 0.1$ $K^{-1/2}$, the log of the resistance has a linear dependence on $T^{-1/2}$, and for $T \leq 100$ K, the resistance is weakly dependent on temperature. So we believe, below 100 K, the conduction is mainly due to tunneling between localized states, and above 100 K, mainly due to thermally activated hopping.

The measured temperature coefficient of resistivity (α) at 300 K for this film is -0.01 K^{-1}. Though this value of α is favorable for obtaining a high voltage responsivity, we have found that the NEP of the microbolometer is limited by the 1/f noise upto 50 kHz. Moreover, its NEP is much greater than that of the Nb microbolometer with similar dimensions [13].

It has been reported that annealing can have substantial effects on the 1/f noise properties of metallic films [34]. So, I annealed the microbolometer in the rapid thermal annealing (RTA) system at 300^0 C for five minutes, and not surprisingly, after annealing, I found that the microbolometer showed a metallic behavior with $\alpha = 0.001$ K^{-1} at 300 K. For all the microbolometers that I annealed, their resistance decreased by $20\% - 30\%$ which can be seen by comparing the dV/dI vs. V plots shown in Fig. 4-1. The 1/f noise level of the microbolometer also decreased approximately by an order of magnitude. We believe annealing removed some of the defects from the Nb films and also improved the ohmic contacts between the gold and Nb films. The DC I-V and dV/dI vs. V plots of the Nb microbolometer after annealing is shown in Fig. 4-1(b).

We deduce the voltage responsivity of the Nb microbolometer by using Eq. 4.1, and it is shown in Fig. 4-3. The I-V curve of the same device is provided in the inset.

4.2 Frequency Response

The frequency response of a detector provides the information on how fast it can follow a detected signal. From Eq. 2.2, we find that due to the small heat capacity of the microbolometer, its frequency dependent voltage responsivity will be determined by its total thermal conductance $G_t(f)$. Using $\kappa_g = 3.17$ $W/cm - K$ for gold at 300
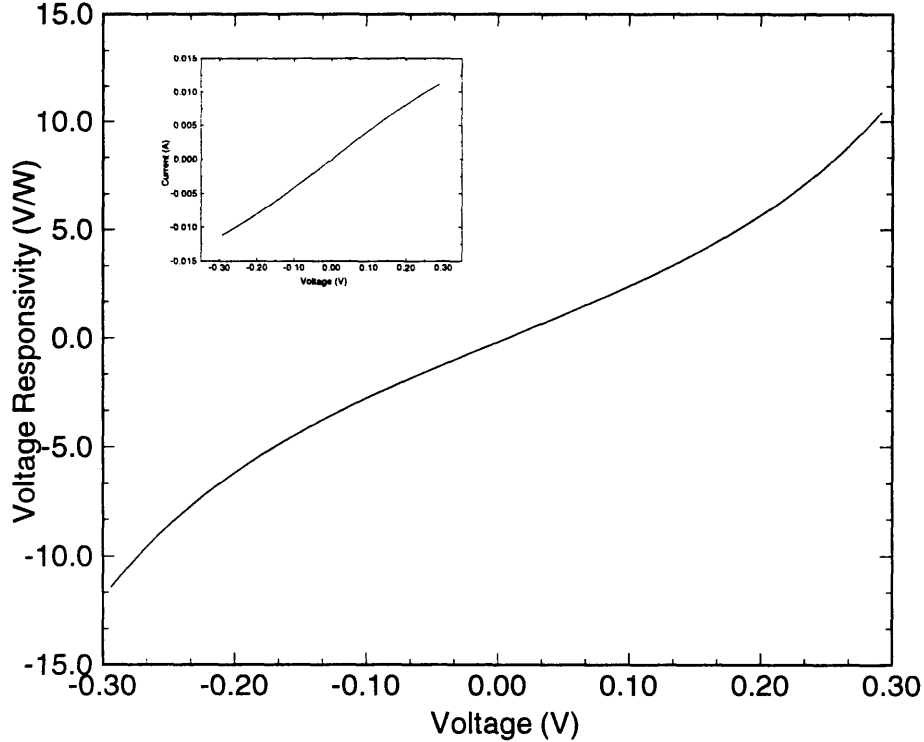
Figure 4-3: Deduced voltage responsivity of a 10 nm micromachined Nb microbolometer after annealing. The I-V curve is shown in the inset.

K [64]. $w = 20\ \mu m$, $t_a = 200\ nm$ and $l = 800\ \mu m$ in Eq. 2.6, we get the DC thermal conductance of the gold leads $G_a = 3.22 \times 10^{-6}\ W/K$. Similarly, the DC thermal conductance of membrane using $r_1 = 1.7\ \mu m$, $r_2 = 800\ \mu m$, $t = 1\ \mu m$ and $\kappa_m = 0.2\ W/cm\ K$ in Eq. 2.3 yield, $G_m = 2.1 \times 10^{-5}\ W/K$. For our device geometry G_c is negligible compared to G_m and G_a. Since $G_m(0)$ is approximately an order of magnitude larger than $G_a(0)$, $G_t = G_m + G_a \simeq G_m$. So, the frequency response of the micromachined microbolometer is dictated by the frequency dependence of the thermal conductance of the membrane. The frequency dependent responsivity can be found from the expression for the temperature variation along the radial direction on the membrane for a point source located at the center of the membrane (Eq. 2.4).

To measure the frequency response of the Nb micromachined microbolometer, we use the experimental setup shown in Fig. 4-4. A Gunn oscillator tuned at 95 GHz is used as the radiation source. It is amplitude modulated with a ferrite modulator [65], and the modulation frequency can be tuned from 10 $Hz - 50\ kHz$. To
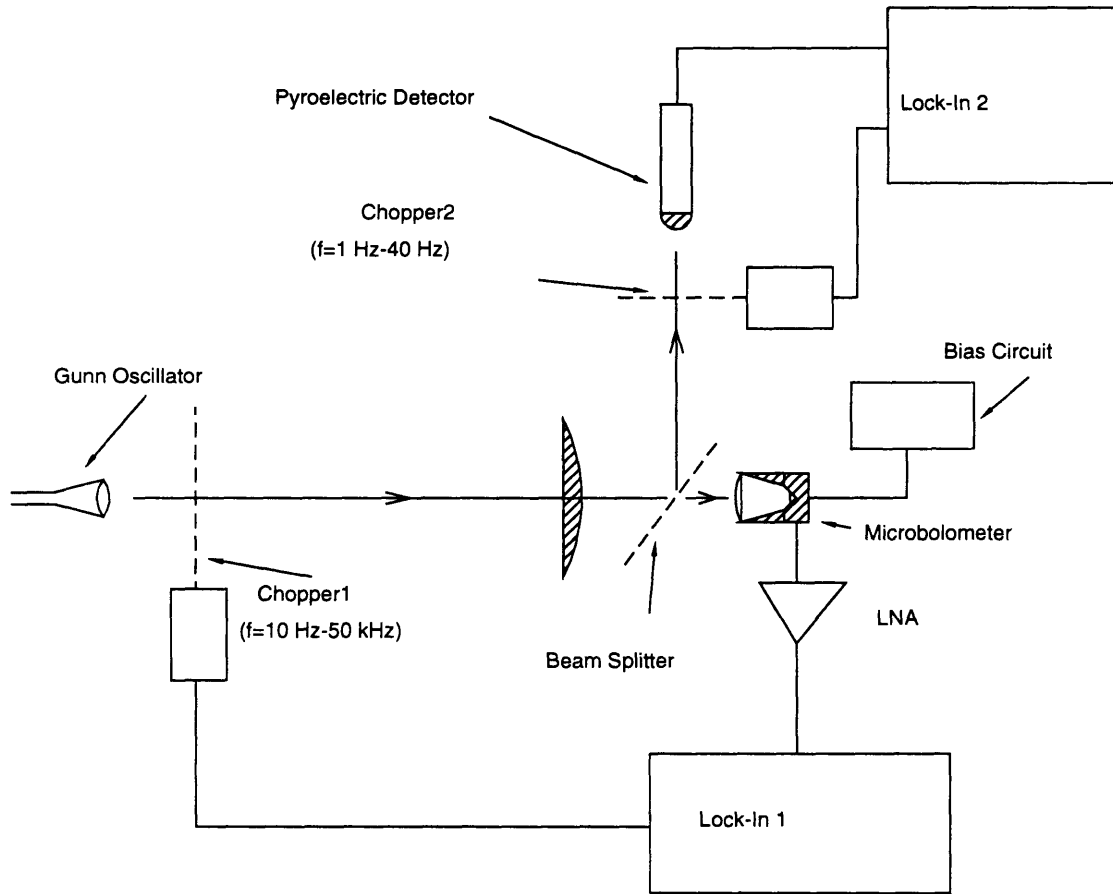
Figure 4-4: The experimental setup used for measuring the frequency response of the micromachined Nb microbolometer.
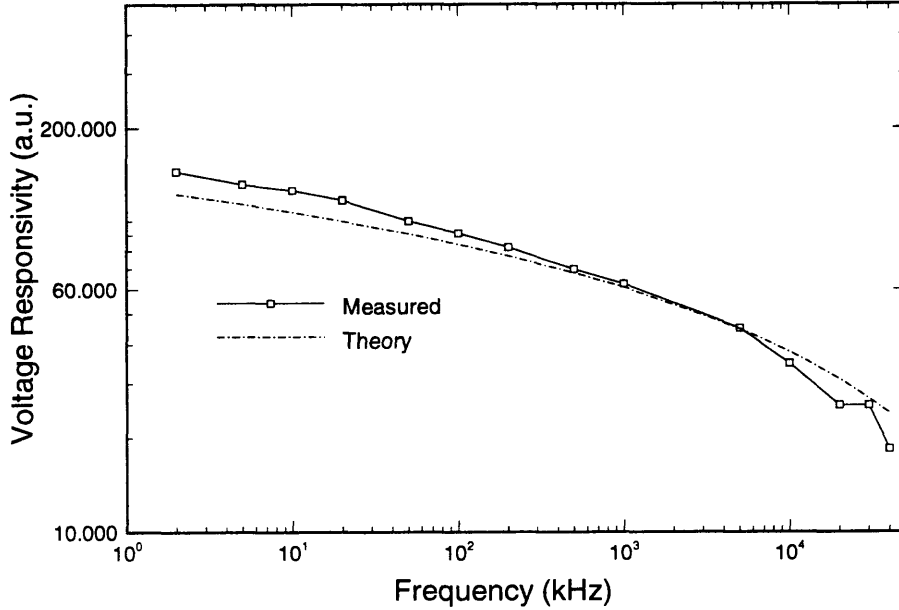
Figure 4-5: Frequency response of a 10 nm-micromachined Nb microbolometer. The calculated values are found by using Eq. 2.4, and the experimental results are obtained with an amplitude modulated Gunn oscillator.

maintain constant incident radiation power at various modulation frequencies, we use an independent pyroelectric detector [16] to measure the average power level. The calculated and experimentally measured frequency response of the microbolometer is shown in Fig. 4-5. The experimental results agree very well with the theory, and the frequency response has a $\ln(1/f)$ dependence with frequency. Therefore, it shows a much slower roll-off with frequency than the f^{-1} behavior of conventional "macro" bolometers.

We define a thermal decay length r_{th} as the distance over which the tempera-ture increase in the membrane drops to 10% of the temperature increase ΔT in the bolometer, and it is given by $r_{th} \simeq 0.6(\kappa/2\pi f)^{1/2}$. The transition from steady state (Eq. 2.3) to a frequency dependent conductance (Eq. 2.4) will then occur at a fre-quency where $r_{th} \simeq r_2$. As the modulation frequency increases beyond this point, the effective thermal decay length is smaller than r_2, resulting in a higher value of thermal conductance than that given by Eq. 2.3. Calculation for the square membrane indi-

cates that this frequency is approximately 2 Hz. So, Eq. 2.3 is a good representation of the thermal conductance of the membrane from $0 - 2$ Hz.

4.3 Noise Equivalent Power (NEP)

As discussed in chapter 2.2, NEP determines the sensitivity of a microbolometer. To measure the electrical NEP, the microbolometer is biased with a current source, and the noise voltage across it is amplified with a low noise amplifier (LNA). This amplified signal is then measured with a spectrum analyzer.

The noise voltage that we attempt to measure is in the range of $0.5-1.5$ $nV/Hz^{1/2}$. So, the noise floor of the amplifier must be smaller than this. For the PAR-13 amplifiers which are available in our lab., its noise voltage is ~ 6 $nV/Hz^{1/2}$; so they cannot be used to directly amplify the noise signal. A commonly used technique for measuring the noise signal of low resistance source is transformer coupling. A transformer can be used to change the resistance of a source seen by the LNA to match the LNA's optimum resistance [28, 30]. This type of transformer-coupled system has a roll-off frequency in the range of 5 $kHz - 10$ kHz; so they are not useful for broadband noise measurements.

We can also measure the noise voltage using noise-correlation method [28]. The principle behind it is as follows: First, the noise signal is fed into two parallel amplifiers. Then the two amplified signals s_1 and s_2 are fed to a cross correlator which outputs a signal proportional to $s_1 s_2$. Now the average $\overline{s_1 s_2}$ is measured. In the averaging process, the two amplifiers' noise terms drop out because they are uncorrelated, and only the noise signal term remains. The circuits that implement the noise correlation are very complex. After evaluating the complexity and limitation of all these noise measurement techniques, I decided to build a LNA by using very low noise BJT MAT-02 [66]. The circuit diagram of the low-noise voltage preamplifier is provided in Appendix C. The gain of the preamplifier is ~ 100, and the noise signal is amplified further by a PAR-13 amplifier with its gain set to 10. The amplified noise signal is measured with a spectrum analyzer.
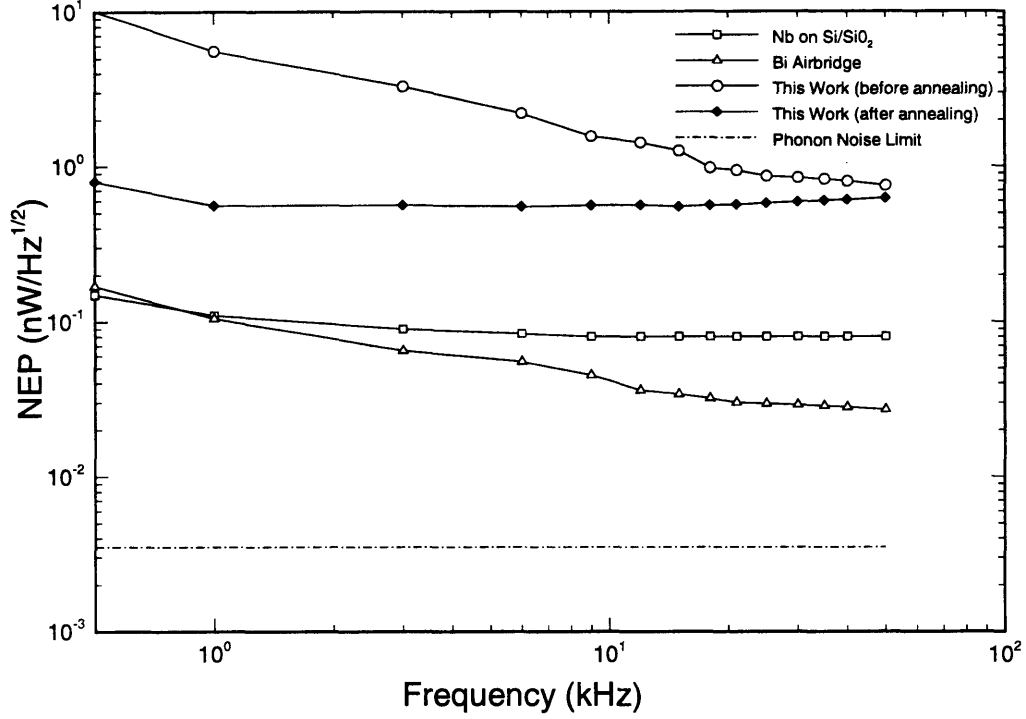
Figure 4-6: Electrical noise equivalent power of a micromachined Nb microbolometer before and after annealing. These are also compared with the NEP of a Nb and air-bridge Bi microbolometer [11, 13]. The dash-dotted line is the fundamental limit of the NEP, set by the phonon noise.

Following the noise model of a resistor R_s connected with an amplifier with gain G which is presented in Sec. 2.2, the amplifier's input noise is given by:

$$E_{in} = E_{out}/G$$

$$= [(I_n R_s)^2 + E_n^2 + 4kTR_s]^{1/2}. \tag{4.3}$$

By short circuiting the amplifier's input terminals ($R_s = 0$) and by measuring the output noise voltage, we can deduce the amplifier's noise voltage E_n. Once we know E_n, we can measure the output noise voltage for a known source resistance, and use Eq. 4.3 to deduce the amplifier's noise current I_n. The measured noise voltage of the amplifying stage is 1.1 $nV/Hz^{1/2}$, and the noise current is 2.8 $pA/Hz^{1/2}$.

The electrical noise equivalent power of a 10-nm micromachined Nb microbolome-

ter both before and after annealing is shown in Fig. 4-6. The NEP before annealing the device is dominated by the 1/f noise up to 50 kHz. After annealing, with a total resistance of the microbolometer $R_t = 60\ \Omega$ (30 Ω for the bolometer and 30 Ω for the bias contact leads) and a bias current of 3.6 mA (which corresponds to a voltage responsivity $S = 5\ V/W$), contributions from different noise sources to the NEP are $\sqrt{4KTR_t}/S = 2.0 \times 10^{-10}\ W/Hz^{1/2}$, $\sqrt{4KT^2G_t} = 1.1 \times 10^{-10}\ W/Hz^{1/2}$, and $\sqrt{e_n^2 + (i_nR_t)^2}/S = 2.2 \times 10^{-10}\ W/Hz^{1/2}$. The measured contribution from the 1/f noise sources to NEP at 1 kHz is $3.2 \times 10^{-10}W/Hz^{1/2}$. The NEP is dominated by the amplifier's noise and Johnson noise for $f \geq 3\ kHz$, and by the 1/f noise below 3 kHz.

The micromachined Nb microbolometer examined in this chapter is not yet optimized for the best NEP. The NEP can be reduced further by fabricating the microbolometer on a cross-shaped structure which is shown in Fig. 3-8. Moreover, we can also reduce the thickness of the Si_3N_4 membrane to increase the thermal isolation to the microbolometer. With a $0.5-\mu m$ thick Si_3N_4 membrane of a cross geometry, we can reduce the thermal conductance of the membrane to $4.6 \times 10^{-6}\ W/K$. This will correspond to an overall NEP of $1.56 \times 10^{-11}\ W/Hz^{1/2}$. This is sensitive enough to detect blackbody radiation $kTB = 6.2 \times 10^{-11}\ W$ for a 1 sec. integration time. Here, we have assumed a system bandwidth $B = 15\ GHz$ and room temperature operation. This new design idea to reduce the NEP, at least, by an order of magnitude is incorporated with the new batch of microbolometer fabrication.

4.4   Summary

In this chapter the experimental results for the micromachined Nb microbolometer are presented. Uncertainties about the microbolometer-film quality and characteristics are resolved by systematic measurements and analyses. New design ideas are also discussed to reduce the overall NEP of the micromachined Nb microbolometer.

The experimental results on the frequency response and electrical noise equivalent power of the micromachined Nb microbolometer was published in Appl. Phys. Lett.

65

68(14), 2020, 1996.

Chapter 5

Conclusion and Future Work

5.1 Conclusion

In this thesis, we have presented the design, fabrication and characterization of un-cooled micromachined Nb microbolometers. Our motivation for developing mm-wave micromachined microbolometers is their compact size, light weight, and inexpensive fabrication process. We have achieved electrical noise equivalent power of 4.5×10^{-10} $W/Hz^{1/2}$ at 1 kHz modulation frequency with the micromachined Nb microbolometer. We have found that for our device geometry, thermal conduction through the Si_3N_4 membrane is the most dominant thermal conduction path. To reduce the thermal conductance of the membrane in future designs, new design ideas based on Si-micromachining have been proposed.

Design requirements of an imaging array using micromachined microbolometers have been discussed in details. During the characterization of the Nb microbolometer, we encountered an unusual dependence of the bolometer-film's resistance with temperature. This unusual behavior have been explained by analyzing the $\ln(R)$ vs. $T^{-1/2}$ and $I - V$ plots of the Nb microbolometer. We have demonstrated that thermal annealing could improve the ohmic contacts between the gold and the niobium films and reduce the 1/f noise level of the microbolometer. Some of the important features of the uncooled Nb microbolometer is summarized in the following table.

DC resistance	$25 - 45\ \Omega$
Voltage responsivity	$4 - 6\ V/W$
Total DC thermal conductance	$\sim 2 \times 10^{-5}\ W/K$
Noise Equivalent Power	$4.5 \times 10^{-10}\ W/\sqrt{Hz}$ at 1 kHz

5.2 Future Work

This thesis work has emphasized the advantages of micromachined structures for developing mm-wave detectors and focal plane arrays. Currently, our primary goal is to design and fabricate sensitive microbolometers by means of Si-micromachining and to use them for developing mm-wave focal plane imaging arrays. We would like to increase the sensitivity of these microbolometers further by implementing several ideas discussed in Sec. 4.3.

In future, for optimizing the performance of the micromachined microbolometer, we must address both material (radiation absorber and temperature sensor film) and radiation coupling related issues. For material related issues, we should explore if any other materials with large temperature coefficient of resistivity (α) but small 1/f noise level can be used as the radiation absorber and the temperature sensor. It is well known that phase transition of materials can be exploited to detect electromagnetic radiation [67]. Due to the large α near the phase transition temperature, these materials are ideal as temperature sensors for bolometers [67, 68]. Vanadium dioxide (VO_2) has a metal-semiconductor phase transition at $68^0\ C$ [69]. This transition, with increasing heat input to the VO_2 film, is from semiconductor phase to the metal phase. So, VO_2 film can be used as the temperature sensor for bolometric detection by biasing it near its transition temperature. Since the transition temperature is $68^0\ C$, VO_2-bolometers will operate at room temperature. Before contemplating on the design and fabrication of VO_2-microbolometers, we should study thoroughly the VO_2-film deposition process and its compatibility with the micromachined structures, and its noise properties.

Another issue that needs to be addressed is the array spacing of the microbolometers for the focal plane imaging arrays. It has been discussed in Sec. 2.4.2 that in the

current design, we undersample at the focal plane, and the sampling interval is set by the aperture size of the machined horn. To correct the undersampling, we need to design new type of machined horn section (conical or corrugated horn) with smaller flare angle without sacrificing antenna gain so that the constrains on the sampling interval set by machined horn's aperture size will be reduced.

Appendix A

Modified Bessel Function

Modified Bessel function $K_v(z)$ is the solution of the differential equation of the form

$$z^2 \frac{d^2 w}{dz^2} + z \frac{dw}{dz} - (z^2 + v^2)w = 0. \tag{A.1}$$

$K_v(z)$ tends to zero as $|z| \to \infty$ for $|arg\ z| < \frac{\pi}{2}$. In the lower limit of z, for $z \to 0$, $K_0(z) \sim -\ln z$. $K_0(z)$ is expressed in terms of $ker(z)$ and $kei(z)$ functions as $K_0(z) = ker(z) + ikei(z)$. Polynomial approximation for $ker(z)$ and $kei(z)$ are given below [24]:

$$
\begin{aligned}
ker(z) &= -\ln(z/2)ber(z) + \pi/4 \cdot bei(z) - .57721566 - 5905819744(z/8)^4 \\
&\quad 171.36272133(z/8)^8 - 60.60977451(z/8)^{12} + 5.65539121(z/8)^{16} \\
&\quad -.19636374(z/8)^{20} + 0.00309699(z/8)^{24} - .00002458(z/8)^{28} + \epsilon \\
&\quad |\epsilon| < 1 \times 10^{-8} \\
&\quad \text{for } 0 < z \le 8 \\
kei(z) &= -ln(z/2)bei(z) - \pi/4 \cdot ber(z) + 6.76454936(z/8)^2 - 142.91827687(z/8)^6 \\
&\quad 124.23569650(z/8)^{10} - 21.30060904(z/8)^{14} + 1.17509064(z/8)^{18} \\
&\quad -.02695875(z/8)^{22} + 0.00029523(z/8)^{26} + \epsilon \\
&\quad |\epsilon| < 3 \times 10^{-9}
\end{aligned}
$$

for $0 < z \leq 8$

where $ber(z)$ and $bei(z)$ are written as:

$$ber(z) = 1 - \frac{(z^2/4)^2}{(2!)^2} + \frac{(z^2/4)^4}{(4!)^2} - \ldots\ldots$$

$$bei(z) = z^2/4 - \frac{(z^2/4)^3}{(3!)^2} + \frac{(z^2/4)^5}{(5!)^2} - \ldots\ldots$$

Appendix B

Autocad Drawing Files for Mask Generation

The tables in this appendix list all the BLOCKS (drawing files) that are generated in Autocad for mask layout. These tables are organized as follows: The BLOCKS for a single element (antenna, bolometer definition etc.) are listed in column 3. These BLOCKS are inserted into the BLOCKS listed in column 1 to create arrays of antennas, bolometers etc. The array files are then inserted into *.DXF files listed in colum 2 to produce the final maks layout files.

Array Files	Mask Layout Files (*.DXF)	Single Element-BLOCKS
m95antenn.dwg	mask1.dxf	m95ant.dwg, 95markant.dwg
m95ap1.dwg	mask4.dxf	95bap1.dwg
m95ap2.dwg	mask4.dxf	95bap2.dwg
m95ap3.dwg	mask4.dxf	95bap3.dwg
m95ap4.dwg	mask4.dxf	95bap4.dwg
m95apd.dwg	mask3.dxf	95bapd.dwg, 95mrkirapd.dwg
m95bapx60.dwg	mask6.dxf	95bapx60.dwg, 95markant.dwg
m95bol.dwg	mask2.dxf	95markirbol.dwg, 95markbol.dwg
		95bolcap1.dwg, 95bolcap2.dwg
		95bolcap3.dwg, 95bolcap4.dwg

Array Files	Mask Layout Files (*.DXF)	Single Element-BLOCKS
m190antenna.dwg	mask3.dxf	m190antn.dwg, 190markant
m190ap1.dwg	mask1.dxf	190bap1.dwg
m190ap3.dwg	mask1.dxf	190bap3.dwg
m190ap4.dwg	mask1.dxf	190bap4.dwg
m190apd.dwg	mask2.dxf	190bapd.dwg, 190marirapd.dwg
m190bapx120.dwg	mask2.dxf	190bapx120.dwg, 190markant.dwg
m190bapx60.dwg	mask3.dxf	190bapx60.dwg, 190markant.dwg
m190bolcap.dwg	mask2.dxf	190markbol.dwg, 190markirbol.dwg
		190bolcap1.dwg, 190bolcap2.dwg
		190bolcap3.dwg, 190bolcap4.dwg

Table B.1: List of all the BLOCKS and mask layout files for the 90 GHz and 190 GHz microbolometers. The first table is for the 95 GHz, and the second table is for the 190 GHz microbolometers.

Appendix C

Low Noise AC-Coupled Voltage Amplifier

A modified version of the low noise amplifier (LNA) described in Ref. [30] is used to amplify the noise signals for electrical NEP measurements. MAT-02 BJTs [66] which have a very low noise voltage ($0.9 - 1.0$ $nV/Hz^{1/2}$ at 1 kHz) are used to build the AC-coupled LNA. Circuit diagram of the LNA is shown in Fig. C-1. For the LNA, measured input noise voltage is 1.1 $nV/Hz^{1/2}$ and noise current is 2.8 $pA/Hz^{1/2}$.

The collector current in each BJT is approximately $(1.6 - 0.65)V/6R_3 = 0.8$ mA. For this value of collector current, $g_m = 0.03$ Ω^{-1} and $r_{o'} \sim 5.5$ $K\Omega$. So, the small signal voltage gain is $\simeq 3g_m(r_{o'}\|R_8) = 106$. The voltage gain that I measured was ~ 101.
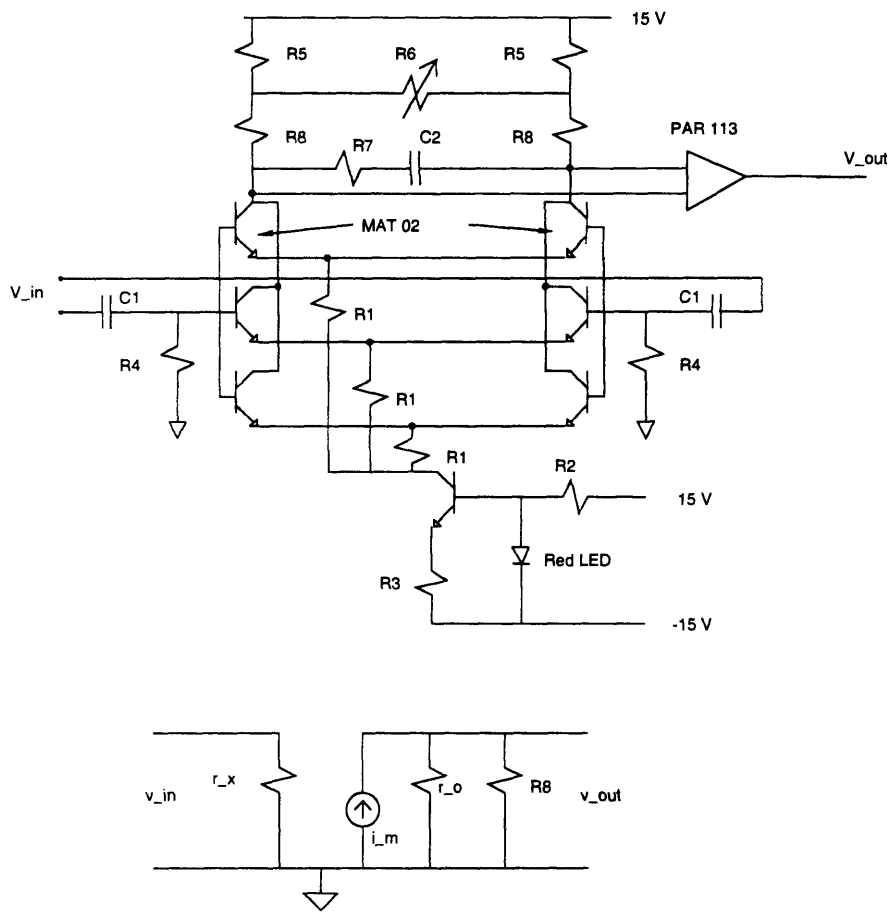
Figure C-1: Circuit diagram and the small signal model of the AC-coupled LNA amplifier that is used for the noise measurment. The preamplifier has a gain of ~ 100, and the noise signal is amplified further by a PAR 113 amplifier with its gain set to 10. The values of all the resistors and capacitors are: $R1 = 390\ \Omega$, $R2 = 27\ k\Omega$, $R3 = 200\ \Omega$, $R4 = 10\ k\Omega$, $R5 = 22\ \Omega$, $R6 = 100\ \Omega$, $R7 = 150\ \Omega$, $R8 = 1.5\ k\Omega$, $C1 = 10\ \mu F$, and $C2 = 200\ pF$. In the small signal model, $r_x = r_\pi/3$, $i_m = 3g_m v_\pi$, and $r_{o'} = r_o/3$.

Appendix D

Device Fabrication Steps

All the fabrication steps for the micromachined Nb microbolometers are provided in the following pages:

Step 1: Wafer Dicing

—   Clean wafers in ACE 5 min/MEOH 5 min/DI. TCE cleaning at 70^0 C
is necessary if there is any grease in the wafer

—   Spin FSCM at 3000 rmp for 30 s.

—   Bake at 120^0 C for 1 min.

—   Dice the 4" round wafers to 2" and 3" diagonal squares

Step 2: Nb Film Deposition and the Nb Strip Patterning

—   Strip FSCM in ACE (5 min)

—   Clean wafers (ACE 5 min/MEOH 5 min/DI)

—   Plasma Ash (1 min)

—   Sputter Nb film on the device wafers and test structures

—   Measure R vs. T on the test structures

—   Clean wafers (ACE 5 min/MEOH 5 min/DI)

—   Plasma Ash (1 min)

—   Vapor HMDS (10 min)

—   Spin 1470 at 4000 rpm for 30 s

—   Bake at 120^0 C for 2 min in the hot plate

— Clean the backside of the device wafer with ACE

— Expose (3.3 s, HP mode)

— Develop with 452 for 40-50 s until all the patterns are visible

— Plasma Ash (1 min)

— Plasma Etch Nb ($\sim 3\ min$)

— Strip resist and clean the wafer

— Inspect under the microscope .

Step 3: IR Alignment and Aperture Definition

— Clean wafers/plasma ash 1 min/vapor HMDS 10 min

— Spin FSCM at 3000 rmp for 30 s on the device side of the wafer

— Spin 5218 at 4000 rpm for 30 s on the back side of the wafer

— Bake at $100^0\ C$ on vac. hot plate

— Use the IR aligner in Group 84's fabrication lab; expose for 20 s

— Bring the wafers to Group 86's clean room and bake at $120^0\ C$ for 1.5 min

— Flood expose for 90 s

— Develop with MIF 422

— RIE etch Si_3N_4 on the back side of the device wafer to define the square windows (all the unwanted structures must be covered with PR)

— Remove the mounting grease

— Clean wafers

Step 4: SiO Deposition

— Clean wafers/plasma ash/Vapor HMDS

— Spin AZ 5218 at 4000 rpm for 30 s

— Bake at vac. hot plate at $100^0\ C$

— Expose 3.2 s (HP mode)

— Bake at $120^0\ C$ for 1.5 min

— Flood expose 90 s (soft contact mode)

— Develop with MIF 422

—   Thermally evaporate 150 nm-200 nm SiO

—   Lift off SiO

—   Inspect under the microscope

Step 5: Antenna/ Gold metallization

—   Clean wafers/plasma ash (1 min)/ vapor HMDS

—   Spin AZ 5218 at 4000 rpm for 30 s

—   Bake at vac. hot plate at 100^0 C

—   Expose 3.2 s (HP mode)

—   Bake at 120^0 C for 1.5 min

—   Flood expose 90 s (soft contact mode)

—   Develop with MIF 422

—   Thermally evaporate 200-nm gold and 10-nm titanium.

—   Gold Lift off (keep the wafer in ACE for 3-5 min; then place it in the
ultasonic with the gold side facing down)

—   Inspect under the microscope

—   Measure R vs. T by placing the device wafer in a hot plate and by monitoring
the resistance with a digital multimeter

Step 6: '+' Fabrication

—   Clean wafers/ACE/MEOH/plasma ash/HMDS

—   Spin 1470 at 4000 rpm for 30 s

—   Pattern the '+' (HP mode/ 3.3 s)

—   Develop with developer 452

—   KOH etch through the back side of the device wafer.
First, at 80^0 C for 4.5 hours, then at 65^0 C for one hour

—   Etch Si_3N_4 to define the '+' (use grease to mount the device wafer)

—   Evaporate gold on the side walls/use shadow mask

Step 7: Aperture Fabrication

—   Pattern the appropriate square windows on 2-inch Si wafers.

—   RIE etch (9 - 10 min)

—   KOH etch 4-8 hours

- Evaporate gold on the aperture side walls

- Stack 4-5 anisotropically KOH-etched Si wafers to form the micromachined horn antenna

Bibliography

[1] Holger H. Meinel. Commercial applications of millimeterwaves, history, present status, and future trends. *IEEE Trans. on MTT*, 43(7):1639, 1995.

[2] John E. Carlstrom and Jonas Zmuidzinas. Millimeter and submillimeter techniques. In W. R. Stone, editor, *To appear in Reviews of Radio Science*. The Oxford University Press, 1996.

[3] G. M. Rebeiz, D. P. Kasilingam, P. A. Stimpson, and D. B. Rutledge. Monolithic millimeterwave two-dimensional horn imaging arrays. *IEEE Trans. on Antenna Propagation*, 38:1473, 1990.

[4] G. V. Eleftheriades, W. Y. Ali-Ahmad, L. P. Katehi, and G. M. Rebeiz. Millimeter-wave integrated-horn antennas part I:Theory. *IEEE Trans. on Antenna Propagation*, 39:1575, 1991.

[5] G. V. Eleftheriades and G. M. Rebeiz. High-gain step-profiled integrated diagonal horn-antennas. *IEEE Trans. on MTT*, 40:801, 1992.

[6] W. Y. Ali Ahmad, G. M. Rebeiz, W. L. Bishop, and T. W. Crowe. An 86-106 GHz quasi-integrated low noise Schottky receiver. *IEEE Trans. on MTT*, 41:558, 1993.

[7] Gert de Lange, Brian R. Jacobson, and Q. Hu. A low-noise micromachined millimeter wave heterodyne mixer with Nb superconducting tunnel junctions. *Applied Physics Letters*, 68:1862, 1996.

[8] E. Garcia, B. R. Jacobson, and Q. Hu. Fabrication of high quality superconductor-insulator-superconductor junctions on thin Si_3N_4 membranes. *Applied Physics Letters*, 63:1002, 1993.

[9] Curtis C. Ling and G. M. Rebeiz. A wideband monolithic submillimeter-wave quasi-optical power meter. In *Proceeding of the First International Symposium on Space Terahertz Technology*, 1990.

[10] Arifur Rahman, Gert de Lange, and Qing Hu. Micromachined room-temperature microbolometes for millimeter-wave detection. *Applied Physics Letters*. 68(14):2020, 1996.

[11] D. P. Neikirk, W. W. Lam, and D. B. Rutledge. Far-infrared microbolometer detecors. *International Journal of Infrared and Millimeter-Waves*, 5:245, 1984.

[12] M. B. Weissman. 1/f noise and other slow, nonexponential kinetics in condensed matter. *Rev. of Mod. Physics*, 60:537, 1988.

[13] M. E. MacDonald and E. N. Grossman. Niobium microbolometers for far-infrared detection. *IEEE Trans. on MTT*, 43:893, 1995.

[14] Paul L. Ricahrds. Bolometers for infrared and millimeter wave detection. *Journal of Applied Physics*. 76:1, 1994.

[15] N. W. Ashcroft and N. D. Mermin. *Solid State Physics*. Sanders College Publishing. 1976.

[16] Model P-41 pyroelectric detectors, Molectron Corp., Sunnyvale, California.

[17] Tien-Lai Hwang, S. E. Schwarz, and D. B. Rutledge. Microbolometers for infrared detection. *Applied Physics Letters*, 34(11):773, 1979.

[18] D. E. Pober. Superconducting terahertz mixer using a transition-edge microbolometer. *Applied Physics Letters*, 62:2119, 1993.

[19] A. Skalare, W. R. McGrath, B. Bumble, H. G. LeDuc, P. J. Burke, A. A. Verheijen, and D. E. Prober. Noise temperature and IF bandwidths of a 530 GHz diffusion-cooled hot electron bolometer mixer. In *Proceeding of the Sixth International Symposium on Space Terahertz Technology*, 1995.

[20] William R. McGrath. Hot-electron bolometer mixers for submillimeter wavelengths: An overview of recent developments. In *Proceeding of the Sixth International Symposium on Space Terahertz Technology*, 1995.

[21] D. B. Rutledge, D. P. Neikirk, and D. P. Kasilingam. Integrated-circuit antenna. *Infrared and Millimeter Waves*, 10:1, 1983.

[22] Dean P. Neikirk and David B. Rutledge. Air-bridge microbolometer for far-infrared detection. *Applied Physics Letters*, 44:153, 1984.

[23] H. S. Carslaw and J. C. Jaeger. *Conduction of Heat in Solids*. Claredon Press, 1959.

[24] M. A. Abramowitz and I. A. Stegnn. *Handbook of Mathematical Functions and Mathematical Tables*. Dover Publications, New York, 1970.

[25] Symposium Proceeding on Heat and Mass Transfer by Combined Forced and Natural Convection. pages 8 and 40: 1972, Westminister, London.

[26] J. B. Johnson. Thermal agitation of electricity in conductors. *Phys. Rev.*, 32:97, 1928.

[27] Nyquist. Thermal agitation of electric charge in conductors. *Phys. Rev.*, 32:110, 1928.

[28] Aldert van der Zeil. *Noise in Solid State Devices and Circuits*. John Wiley and Sons, 1986.

[29] Yishay Netzer. The design of low-noise amplifiers. In *Proc. IEEE*, volume 69, page 728, 1981.

[30] C. D. Motchenbacher and J. A. Connelly. *Low-Noise Electronic System Design.* John-Wiley and Sons Inc., 1994.

[31] J. W. Eberhard and P. M. Horn. Excess 1/f noise in metals. *Physical Review B,* 18(12):6681, 1978.

[32] P. Dutta and P. M. Horn. Low frequency fluctuations in solids: 1/f noise. *Rev. Mod. Phys.,* 53:497, 1981.

[33] F. N. Hooge, T. G. M. Kleinpenning, and L. K. J. Vandamme. Experimental studies on 1/f noise. *Rep. Prog. Phys.,* 44:31, 1981.

[34] D. M. Fleetwood and N. Giordano. Direct link between 1/f noise and defects in metal films. *Physical Review B,* 31(2):1157, 1985.

[35] P. Dutta, P. Dimon, and P. M. Horn. Energy scales for noise process in metals. *Physics Review Letters,* 43(9):646, 1979.

[36] G. V. Eleftheriades, W. Y. Ali-Ahmad, L. P. Katehi, and G. M. Rebeiz. A 20 dB quasi integrated horn antenna. *IEEE Microwave Guided-wave Letters,* 2:73, 1992.

[37] W. Y. Ali-Ahmad. *Millimeter and submillimeter wave integrated horn antenna Schottky receivers.* PhD thesis, Department of Electrical Engineering, The University of Michigan, 1993.

[38] G. V. Eleftheriades. *Analysis and Design of Integrated-Circuit Horn Antennas for Millimeter and Submillimeter-Wave Applications.* PhD thesis, Department of Electrical Engineering, The University of Michigan, 1993.

[39] W. Y. Ali-Ahmad, G. V. Eleftheriades, L. P. Katehi, and G. M. Rebeiz. Millimeter-wave integrated-horn antennas part II:Experiment. *IEEE Trans. on Antenna Propagation,* 39:1582, 1991.

[40] K. Sigfried Yngvesson. Near millimeter imaging with integrated planar receptors: general requirements and constrains. *Infrared and Millimeter Waves,* 10:91, 1983.

[41] Paul F. Goldsmith. Designing quasioptical systems. Internal Publication, Millitech Corporation.

[42] Hermann A. Haus. *Waves and Fields in Optoelectronics*. Printice-Hall Inc, New Jersey, 1984.

[43] Paul F. Goldsmith, C. T. Hsieh, G. R. Huguenin, J. Kapitzky, and E. L. Moore. Focal plane imaging systems for millimeter wavelengths. *IEEE Trans. on MTT*, 41:1664, 1993.

[44] Paul F. Goldsmith. Quasi-optical techniques at millimeter and submillimeter wavelengths. *Infrared and Millimeter Waves*, 6:277, 1982.

[45] L. D. Dickson. Characteristics of a propagating Gaussian beam. *Applied Optics*. 9(8):1854, 1970.

[46] K. S. Yngvesson, J. F. Johansson, Y. Rahmat-Samii, and Y. S. Kim. Realizable feed-element patters and optimum aperture efficiency in multibeam antenna systems. *Trans. on Antenna and Propagation*, 36:1637, 1988.

[47] Verginia Semiconductor Inc., Fredericksburg, VA. Phone #: 540-373-2900. Person to Contact: Perry Cook.

[48] Center for Integrated System, Standford University, CA. Phone #: 415-725-6727. Person to Contact: Nancy Latta.

[49] Shipley Company, Inc. Phone #: 800-345-3100. Person to Contact: Karen Ambrogi. Positive photoresist 1470 and 4620, negative photoresist 5218 and 5214 and non-photoactive resist FSCM can be purchased from Shipley.

[50] R. K. Hoffmann. *Handbook of Microwave Integrated Circuits*. Artech House, Massachesetts, 1987.

[51] Carl T. A Johnk. *Engineering Electromagnetic Fields and Waves*. John-Wiley and Sons Inc. New York, 1988.

[52] Autocad reference manual, Release 11. Autodesk Ltd., England, August 1990.

[53] Photronics, Brookfield, CT. Phone #: 203-775-9000. Person to Contact: Robert S. Anderson.

[54] K. E. Petersen. Silicon as a mechanical material. In *Proceedings of the IEEE*, volume 70, page 420, 1982.

[55] Brian R. Jacobson. A micromachined SIS mixer. Master's thesis, Department of Electrical Engineering and Computer Science, Massachusetts Institue of Technology, 1994.

[56] Custom Microwave, Longmount, CO. Phone #: 303-651-0707. Person to Contact: Mike Larson.

[57] J. F. Johansson and N. D. Whyborn. The diagonal horn as a sub-millimeter wave antenna. *IEEE Trans. on MTT*, 40:795, 1992.

[58] Robert W. Hass, Bennis Brest, Harry Mueggenberg, Lee Lang, and Dave heimlich. Fabrication and performance of MMW and SMMW platelet horn array. *International Journal of Infrared and Millimeter-Waves*, 14:2289, 1993.

[59] R. C. Jones. The general theory of bolometer performance. *Journal of Optical Society of America*, 43:1, 1953.

[60] Edward Riley Pollard Jr. *Electronic Properties of niobium monoxide*. PhD thesis. Department of Material Science, Massachusetts Institute of Technology, 1968.

[61] E. H. Greener and D. H. Whitemore. Electrical conductivity of near-stoichiometric $\alpha - Nb_2O_5$. *Journal of Chemical Physics*, 34(3):1017, 1961.

[62] Sir Nevill Mott. *Conductivity in Non-Crystalline Materials*. Oxford Science Publications, Oxford, 1987.

[63] Hiroshi Kamimura and Kideo Aoki. *The Physics of Interacting Electrons in Disodreded Systems*. Oxford Science Publications, Oxford, 1989.

[64] CRC Handbook of Chemistry and Physics. CRC Press,Boston, 1995.

[65] Modulator Driver, Model 47530H-511X, Huges.

[66] MAT-02 BJTs manufactured by Analog Devices, Norwood, Mass. were used to buid the LNA.

[67] J. Clare, G. I. Hoffer, P. L. Richards, and N. H. Yeh. Superconductive bolometers for submillimeter wavelengths. *Journal of Appl. Phys.*, 48(12):4865, 1978.

[68] R. S. Scott and G. E. Fredericks. Model for infrared detector by a metal-semiconductor phase trnasition. *Infrared Physics*, 16:619, 1976.

[69] F. J. Morin. Oxides which show a metal-to-semiconductor transition at the Neel-temperature. *Physical Review Letters*, 3:34, 1959.